DoD Center for Geosciences/Atmospheric Research under grant DAAD19-02-2-0005

THE ADDITION OF THE DIRECT RADIATIVE EFFECT OF ATMOSPHERIC AEROSOLS INTO THE REGIONAL ATMOSPHERIC MODELING SYSTEM (RAMS)

by David Stokowski

William R. Cotton, P.I.

Colorado State University

Department of Atmospheric Science

Paper No. 764

The Addition of the Direct Radiative Effect of Atmospheric Aerosols into the Regional Atmospheric Modeling System (RAMS)

BY

David M. Stokowski

Department of Atmospheric Science

Colorado State University

Fort Collins, CO 80523

Research Supported by

Department of Defense Center for Geosciences/Atmospheric Research (CG/AR), under cooperative agreement #DAAD-19-02-2-2005

1 November 2005

Atmospheric Science Paper No. 764

ABSTRACT

Forecasting of the radiative impact of atmospheric aerosol species is one of the largest problems remaining in determining the magnitude of expected climate change over the next century and beyond. While much has been accomplished to achieve this goal, little has been done to this end in regional and mesoscale forecasting models. Models including the aerosol radiative effect would allow for prediction of small-scale visibility degradation features, as well as more complete investigation of the radiative impact of aerosols on everyday weather.

In this project, the direct radiative effect of three atmospheric aerosol species was added to the Regional Atmospheric Modeling System (RAMS). Ammonium sulfate, sea salt and mineral dust were treated in an analogous manner to the hydrometeor species already in RAMS—they are assumed to have a log-normal size distribution, and are allowed to advect within the model. The aerosols are assumed to interact with short- and longwave radiation, using Mie theory as a basis for these interactions. RAMS was set-up using a 2-D LES-type simulation with each model run initialized horizontally homogeneously, using a two second time step, for a total of 78 hours of simulation time. A matrix of

model runs was completed using assumed concentrations of ammonium sulfate and sea salt, with three experimentally determined mineral dust concentration profiles taken from the SaHAran Dust Experiment (SHADE). The effect of the presence of ammonium sulfate was negligible in nearly every field evaluated, while sea salt showed only minor changes to the downwelling longwave radiation profiles, as well as visibility profiles.

The most dramatic changes to the temperature and radiation profiles in the model were due to the radiative activity of mineral dust. First, where the elevated mineral dust concentrations are present, the atmospheric temperature is increased (up to 3°C per day), as mineral dust has a large imaginary part of the refractive index. The downwelling shortwave radiation is also decreased anywhere from 100-470W/m^2 through the dusty layers. Unfortunately this value is upwards of four times too great, as the maximum effect during the SHADE campaign was measured by Haywood, et. al (2003) to be –129 ± 5 W/m^2. Once sensitivity studies looking at the changes in the imaginary part of the refractive index of mineral dust were completed, the maximum downwelling shortwave forcing from the model was reduced to –141W/m^2. The overall prediction of visibility was also in the correct sense, but was not able to be quantitatively tested.

The initial results from this study are qualitatively positive. Once both three-dimensional testing is completed, and more accurate values of the refractive index of aerosol species are available (especially for mineral dust), the quantitative results can be used to check on

specific cases of visibility degradation, as well as how the radiative impact of aerosols will affect everyday weather phenomena.

David M. Stokowski
Department of Atmospheric Science
Colorado State University
Fort Collins, CO 80523
Fall 2005

ACKNOWLEDGEMENTS

I would first like to acknowledge and thank Dr. William Cotton for taking a chance on me as a graduate student, as well as for his continued guidance and insight during the preparation of this paper. Also deserving thanks are Dr. Christian Kummerow and Dr. David Krueger for their time and thoughtful consideration of this work. As Dr. Cotton's research group has been of invaluable help, I would like to thank group members both past and present for imparting their knowledge upon me: Jerry Harrington, for his utmost patience in helping a new user understand the beast that it RAMS; Dr. Graham Feingold whose Mie scattering code forms the foundation of the radiation subroutine added to RAMS: to Dr. Hongli Jiang and Dr. Gustavo Carrio for their assistance in using RAMS as an LES-model; Dr. Susan van den Heever as a guide and giver of sage advice to a master's student; to Steve Saleeby as a constant help and source of scientific discussion, to Liz Zarovy for her help in understanding current avenues of aerosol research, both scientifically and as it relates to RAMS; to R. Todd Gamber and Jeremy Orban for robbing me of the joy of driving to and from Fort Collins, by keeping the RAMS computer network up, and accessible from my home; and to Brenda Thompson whose help saved me countless hours of work, and whose conversations gave me perspective impossible to have gained on my own. I wish to give my deepest gratitude to Jim Haywood of the U.K. Meteorological Office, without whose guidance, patience, help and unlimited access to SHADE data, this project would not have been possible. To Luke

van Roekel, constant friend, intellectual stimulator, technical editor, source of comedy, and keeper of the futon—your friendship and support will mean more to me than you will ever know. To my dearest wife, best-friend and mother our child—Rachel, you are a saint for continuing to support me in these seemingly endless and unconnected endeavors; your love and faith in me brings me to tears. To Benjamin, your innocence and presence have shown me what is truly important. And finally, to my Lord, Jesus Christ; after all of this I now truly understand what Paul wrote in Philippians 4:13 – "I can do all things through Him who strengthens me."

This study was graciously and generously supported by the Department of Defense Center for Geosciences/Atmospheric Research, under cooperative agreement #DAAD19-02-2-0005.

TABLE OF CONTENTS

CHAPTER 1 – INTRODUCTION

1.1 INTRODUCTION TO AEROSOLS

The American Heritage Dictionary defines an aerosol as "a gaseous suspension of fine solid or liquid particles." Meteorologically speaking, an aerosol is commonly defined as only the particulate matter (Seinfeld and Pandis, 1998). There are many types of aerosols that are prevalent in today's atmosphere: ammonium sulfate, sea salt, mineral dust, black carbon from industrial processes, smoke, and the list goes on. Aerosols can be classified in two different manners: they can be divided by causation as either natural or anthropogenic; or by formation as either primary (lofted from the surface) or as secondary (formed in the atmosphere). Mineral dust aerosols are primary aerosols whose mobilization is sensitive to factors including soil moisture and surface wind velocities (Ginoux, et. al, 2001). These mineral dust sources can be both natural, as from deserts, or anthropogenic as from desertification through land-use changes (Myhre and Stordal, 2001; Tegen, et. al, 1996). Similarly, sea salt production is also a function of surface wind speed through formation and subsequent evaporation of "film-" and "jet droplets" (Prupppacher and Klett, 1978). Black carbon has a variety of sources, the most prevalent of which are from biomass burning, and residential fuel burning (Streets, et. al, 2004). In urban areas, emissions from diesel trucks also contribute greatly to the global black carbon burden (Schauer, et. al, 1996). Atmospheric sulfur aerosols (commonly referred

to as sulfates) also have both natural and anthropogenic sources. Anthropogenic sulfates are emitted through industrial processes and fossil fuel burning, and account for approximately 65% of the global sulfate burden (Chin and Jacob, 1996 and Chin, et. al, 2000). Most natural sulfur is emitted as dimethylsulfide (DMS) from phytoplankton, and accounts for the remaining 35% of the global sulfate burden (Chin and Jacob, 1996; Chin, et. al, 2000). Each of these aerosols has some effect on the atmospheric radiation balance, but very few numerical weather prediction models take this effect into account, due to poor knowledge of spatial and temporal sources and sinks of the individual aerosols (Andrews, et. al, 2004; Sokolik and Toon, 1996).

1.2 Importance in Forecasting Aerosols

In recent years, the United States Military has increased its worldwide presence in areas susceptible to rapid changes in visibility due to airborne mineral aerosols. This issue was first documented during Operation Desert Storm in Iraq beginning in 1990, and has continued during Operation Enduring Freedom in both Iraq and Afghanistan since 2001. Kuciauskas, et. al (2003) recognized many of the problems that occurred in Iraq during frequent dust storms in the spring of 2003. From an operational cost standpoint, dust storms can degrade the performance of ground-based vehicles, which therefore require more frequent clean up and maintenance. As dust inhibits visibility, operations using laser-guided munitions are greatly limited. Soldiers "getting lost" in dust storms was also cause for great concern. Minimizing the loss of human-life is paramount in conducting operations in dust storm conditions. The most recent example for the need to accurately forecast dust came in the April 16, 2005 crash of a military helicopter in Afghanistan. It

was reported that low visibility caused by a dust storm was present at the time of the crash, killing 16 people during activities carried out as a part of Operation Enduring Freedom.

The importance of forecasting aerosols is also manifested in the civilian realm. One of the main points in the Executive Summary for Policy Makers of the International Panel on Climate Change's (IPCC) Third Assessment Report is that "[e]missions of greenhouse gases and aerosols due to human activities continue to alter the atmosphere in ways that are expected to affect the climate" (IPCC, 2001). While our understanding of the future climate effects due to the so-called greenhouse gases is high, there is a low level of scientific understanding related to aerosol effects on future climate (IPCC, 2001). In fact IPCC states that the magnitude of the direct aerosol forcing could be on the same order of magnitude as that of the greenhouse gases, but in a negative sense (IPCC, 2001). The presence of aerosols can increase the effective albedo of the planet, through processes such as the Twomey (1977) Effect, where anthropogenic sulfate aerosols would increase the number of cloud droplets for a given water vapor content, causing a greater number of small droplets and hence a more reflective cloud. However, much of the trouble in determining the direct radiative effect of aerosols is that there is a very limited data set containing information about the spatial and temporal gradients of atmospheric aerosols (Andrews, et. al, 2004; Sokolik and Toon, 1996). Despite this, it is thought that ammonium sulfate has an overall cooling effect on Earth (Ramanathan, et. al 2001). Depending on the size and location of mineral dust aerosol particles, they can have either a heating or cooling effect (Sokolik and Toon, 1996), while the anthropogenic forcing of mineral aerosols has been shown to have a cooling contribution (Tegen, et. al, 1996).

Black carbon aerosols most often show a warming contribution to atmospheric forcing (Streets, et. al, 2004; Conant, et. al, 2002). Unfortunately, a literature search yielded no useful published information about the effect of sea salt particles on atmospheric temperature changes.

While many of the more widely known aerosol effects are given in terms of global-scale interactions, any modification to radiation streams within a numerical weather prediction model will have effects on model outputs. A recent modeling study of the presence of a Saharan Dust layer during the Cirrus Regional Study of Tropical Anvils and Cirrus Layers - Florida Area Cirrus Experiment (CRYSTAL-FACE), caused a decrease in modeled total precipitation over a control run with only background concentrations of mineral dust (van den Heever, et. al, 2005). On an ever smaller scale, Miller, et. al (2004) discuss that the presence of a layer of dust will decrease turbulence in the planetary boundary layer, due to decreased down-welling solar radiation, and hence decreased turbulent flux of sensible heat into the boundary layer. This also leads to a decrease in surface winds, through a decrease in downward transport of momentum, and hence a decrease in the amount of dust that can be lofted into the atmosphere (Miller, et. al, 2004). Therefore, in order to increase the accuracy of numerical weather prediction models on any scale, the inclusion of the radiative effects of aerosols is a desirable means toward that end.

1.3 History of Numerical Modeling with Aerosols

Over the past fifteen years, a number of numerical weather prediction models have been modified to allow for prediction on aerosol concentrations as well as their effect on the radiation streams within the parent code. Erickson, et. al (1991) introduced a 3-dimensional global sulfur cycle model to include sulfate aerosol effects on cloud nuclei (CN) concentrations. Their research was able to confirm a strong positive relationship between CN concentrations and sulfate. A few years later, Boucher, et. al (1995) specifically investigated the direct radiative effect due to the sulfur cycle, in a general circulation model (GCM) framework. The testing showed a relatively low sensitivity of changes in energy fluxes to sulfate aerosol size and composition, leading the authors to believe that sulfate concentration may be the only variable necessary to determine a good estimate of the sulfate radiative forcing (Boucher, et. al, 1995).

The initial foray into 3-dimensional modeling containing dust was performed by Joussaume (1990). This global climate model was able to simulate many seasonal dust plumes qualitatively well, while recognizing that many oversimplified parameterizations were used (e.g., dust mobilization from wind speeds). The mineral dust model of Tegen and Fung (1994) became the first to account for dust particle size in radiative forcing calculations, while parameterizing sources and sinks of dust.

In the past few years, modeling with aerosols has become more commonplace, and the scale at which these models are being run is also decreasing. As a recent example, the Georgia Tech/Goddard Global Ozone Chemistry Aerosol Radiation and Transport

(GOCART) model has simulated the sulfur cycle, mineral dust cycle and carbon cycle (e.g., Chin, et. al, 2000; Chin, et. al 2002; Yu, et. al, 2004), to yield their radiative forcing on the global scale. The estimated global annually averaged change in surface radiative forcing is $-9.9W/m^2$ for all atmospheric constituents (Yu, et. al, 2004). On a smaller scale, Qian, et. al, (2003) ran a regional climate model over China and was able to reproduce cooling that has been taking place in China over recent decades. The crux of their paper was that the cooling (up to $-14W/m^2$ or $-1.2°C$) was present when their model accounted for the direct radiative effect of ammonium sulfate, methane sulfonic acid, organic carbon, black carbon, sea salt and soil dust.

1.4 Objective of this Research

The main scientific objective of this research was to modify the Regional Atmospheric Modeling System at Colorado State University (hereafter RAMS) to account for the direct (and semi-direct) effect of atmospheric aerosols. A new module containing the FORTRAN code was created and integrated into the existing RAMS framework. The novelty of this approach is that all previous works on the addition of the direct radiative effect of aerosols to a numerical weather prediction framework were under global or regional climate model frameworks, whereas RAMS specific design is to be a mesoscale forecasting model. This new module updates the bulk optical properties of optical depth (t), single scatter albedo (w) and the asymmetry parameter (g), by combining the aerosol optical properties (aerosol direct effect) with cloud droplet and hydrometeor optical properties. These updated values are fed back into the model, modifying the atmospheric column heating rates and hence influencing the microphysics, constituting the semi-direct

effect. Because the aerosol direct effect is now accounted for, a simple code modification was made to determine a visual range, and hence a new forecast variable has become available. The new code has been tested using real data collected during the SaHAran Dust Experiment (SHADE) campaign, which was conducted over the Cape Verde Islands and other areas to the west of continental Africa. Atmospheric temperature and moisture profiles, values of radiation extinction along with radiation fluxes from RAMS have been compared to measurements made using a C-130 aircraft during SHADE.

The remainder of the paper will be organized in the following manner. A discussion about the history and governing equations of RAMS can be found in chapter 2. Chapter 2 also contains a discussion about the modifications made to RAMS, with details about the use and applicability of Mie scattering theory of radiation as well as the off-line code, which was used to generate the optical property look-up tables employed within RAMS. The goals and specific data used in the validation study from the SHADE campaign are presented in chapter 3. Chapter 4 contains information about the model-testing phase, including detailed set-up information as well as model results. Two simple sensitivity studies on the model results to the initial concentration of sea salt and the assumed absorptivity of mineral dust are the foci of chapter 5. A summary of the work with all pertinent conclusions, along with suggestions for future work can be found in chapter 6.

CHAPTER 2 –THE MODEL

2.1 THE REGIONAL ATMOSPHERIC MODELING SYSTEM (4.3.0)

The Regional Atmospheric Modeling System (RAMS), which was developed at Colorado State University, made its debut under the current architecture in 1991. This work was the merger of three previous mesoscale models: a non-hydrostatic cloud/mesoscale model (Tripoli and Cotton, 1982), a hydrostatic version of the above cloud/mesoscale model (Trembeck 1990) and a mesoscale sea-breeze model (Mahrer and Pielke, 1977). Since its 1991 debut, many updates to RAMS have been made, most of which are documented by Cotton et. al, (2003).

For this study, RAMS version 4.3.0 was used. Large sections of RAMS code will not be discussed, as they were not specifically needed in the development and testing of the new radiation module. RAMS uses non-hydrostatic and Reynolds-averaged momentum and mass continuity equations as described in Tripoli and Cotton (1986). A leap-frog time differencing scheme is used to calculate pressures via the Exner function, with a forward time-differencing scheme used for all other prognosed variables. There are a total of 12 prognosed variables within RAMS: the u, v and w wind components, the ice/liquid water equivalent potential temperature (θ_{il}), the dry air density, total water mixing ratio, and mixing ratios of 6 of the 8 hydrometeor species (rain, snow, pristine ice, hail, graupel and

aggregates). From these variables, pressure, potential temperature, vapor mixing ratio, and cloud mixing ratios (small and large cloud droplet modes) can all be diagnosed.

The RAMS model uses a C grid setup (Arakawa and Lamb, 1981; Randall 1994), allowing for straightforward calculation of the individual components of the vorticity equation. The user can define the grid to be either a Cartesian grid, or a polar stereographic grid. The terrain-following vertical coordinate, σ_z is used in RAMS (Gal-Chen and Somerville, 1975; Clark, 1977). RAMS also has the capability of employing two-way interactive nested grids, where the nested grid contains higher horizontal resolution than its parent. These nested grids may (but are not required to) have enhanced vertical resolution.

The microphysics subroutines in RAMS were first developed and described by Verlinde, et. al (1990). This work showed that analytic solutions to the collection equations were possible if one assumed that the collection efficiencies were constant, allowing for prediction on the mixing ratio and concentrations of any of the hydrometeor categories within RAMS. Walko et. al (1995) describes how this was implemented within the RAMS framework. Later, Meyers et. al (1997) extended this prediction to mixing ratio and number concentrations of each of the hydrometeor species. Most recently, a second cloud droplet mode has been added to RAMS to better represent the dual mode of cloud droplets most often observed in nature (Saleeby and Cotton, 2004). For turbulence parameterizations, RAMS has a variety of user specified turbulence closure schemes to choose from, including the Smargorinsky (1963) deformation-K closure scheme, the

Mellor-Yamada (1982) ensemble-averaged TKE scheme and the Deardorff (1980) scheme, where eddy viscosity is a function of TKE.

Harrington (1997) developed the current radiation subroutines that were modified in this study. The radiation code uses a two-stream structure, computing the upwelling and downwelling components by integrating the azimuthally independent radiative transfer equation and applying the δ-Eddington approximation to solve this equation numerically (Harrington, 1997). These radiation calculations are done on eight broad radiation bands, three in the solar region and five in the near infrared. This eight-band structure was chosen to mimic the treatment of gaseous absorption and Rayleigh scattering of water vapor, carbon dioxide, and ozone of Ritter and Geleyn (1992). The overall scattering of radiation within RAMS also accounts for scattering due to the presence of the eight previously mentioned hydrometeor categories (Harrington, 1997). In order to allow these particles to interact with the radiation, three variables need to be defined: the optical depth (τ), the single scatter albedo (ω) and the asymmetry parameter (g). The optical depth is a proxy for total extinguished radiation, where the single scatter albedo describes what fraction of the extinguished radiation is scattered (absorption is the other assumed extinguishing process), and the asymmetry parameter describes the direction in which radiation is scattered as the intensity weighted average of the cosine of scattering angle (Seinfeld and Pandis, 1998). This information is then used to update the atmospheric heating rate profiles, and hence thermal properties throughout the model.

2.2 Modification to RAMS

The main scientific objective of this research was to add the direct and semi-direct radiative effects of aerosols into RAMS. It was determined that the best way to treat the particles was to assume that they were smooth spherical scatterers and absorbers, so that Mie scattering theory could be applied. Therefore the only required input information is the refractive index of given aerosol particles as a function of the wavelength of the incident radiation, as well as the particle size (usually as a radius) and the wavelength of the radiation involved in the interaction. This allows for direct calculation of the total amount and direction of the extinguished and scattered radiation. Once this aerosol effect was accounted for, it was combined with the optical depth (τ), the single scatter albedo (ω) and the asymmetry parameter (g) from the cloud hydrometeors, giving a new total τ, ω and g. The remainder of this chapter describes the details of the new module containing the aerosol direct effect.

2.2.1 Background on Mie Theory

The interaction of radiation with particles is a problem that has no general analytic solution. However, with a few assumptions about the nature of the radiation-particle interaction, exact solutions can be derived. If there is no change in the wavelength of the radiation interacting with a particle, (otherwise known as elastic scattering), and if the particles causing the radiation to scatter are spherical, then the exact solution can be found using Mie (1908) theory. The elasticity assumption basically means that a photon can either change directions, or be absorbed as a change in internal energy. Since

bonding on the atomic level is beyond the scope of this study, it is reasonable to assume that changes in internal energy of a molecule are manifested solely through temperature changes. There is, however, a small body of research describing the validity of the spherical particle assumption as it relates to mineral aerosols. Pollack and Cuzzi (1980) explain that a mixture of small irregularly shaped particles, are expected to exhibit similar scattering behavior to an equivalent volume of spheres. This breaks down for elongated particles with a large total refractive index (Pollack and Cuzzi,1980). However, Mishchenko et. al (1997) found in a theoretical study, that the optical depth, single scatter albedo and the asymmetry parameter are only slightly different when spherical and non-spherical particles are compared using a known optical depth (i.e., known concentration). It therefore seems plausible to assume that our use of Mie Theory for this application is entirely reasonable.

In order to use Mie theory properly, three key parameters are needed: the wavelength of the incident radiation, the size of particle, and the total complex refractive index (Seinfeld and Pandis, 1998). The first two of these parameters are often used together to create a dimensionless size parameter (radius of particle divided by wavelength of radiation). The complex refractive index insures that wavelength dependent information about the absorption and scattering of the particle is taken into account. Once all of this information is sent to a "canned" Mie scattering routine, values for τ, ω and g can be easily obtained.

2.2.2 THE MIE SUBROUTINES

In order to get optical property values necessary for the RAMS radiation subroutine, a method to calculate these values using Mie theory was needed. The "canned" Mie scattering routine used in this study, called equim_5, was developed by Graham Feingold of the National Oceanographic and Atmospheric Administration (NOAA), [personal communication]. For the equim_5 code, only one input variable is needed, the complex refractive index of each aerosol species, all other necessary variables are internally defined. The refractive indices used in this study were adapted from d'Almeida, et. al (1991).

The equim_5 code was used to model three different aerosol species: ammonium sulfate, sea salt and mineral dust. One of the most convenient features of the equim_5 code allows the aerosol species to be either uniform, or an internal mixture, specifically a shell/core mixture. Ammonium sulfate was the only of the three species to be modeled with an insoluble core—having 10% (by mass) ammonium sulfate on a 90% insoluble core of mineral dust. Sea salt was assumed to have no insoluble core, while mineral dust had no soluble outer coating. The equim_5 code was run for each of these three aerosol species, generating 4 tables each: one containing the extinction coefficient (q_{ext}), one containing the scattering coefficient (q_{scat}), one containing the asymmetry parameter (g_{asym}) and one containing a deliquescence growth factor. The three optical property tables are a function of radiation band, particle size and relative humidity, whereas the deliquescence growth factor table is a function of particle size and relative humidity only.

Again, the only required input to the equim_5 code is the complex refractive index of each aerosol species as a function of wavelength. The particle size, and wavelength of radiation needed for Mie theory calculations are internally defined within the equim_5 code. Initially, the code defines a lower particle size limit at 15nm. From there, bin limits are created by determining the radius of particles for a mass four times greater than the mass at the previous bin limit. In order to best represent the larger particles in the model, seventeen bins were chosen, so that the largest bin limit is at 3.048 microns. Each bin is assigned a representative radius by taking the average of the lower and upper masses for each bin, as determined by the bin limit radii. Next, the radiation bands were chosen to mimic the eight bands currently in RAMS--three in the solar spectrum and five in the near-infrared. Each of the eight radiation bands was split into 100 smaller bands, each with an average wavelength. Now, since specific wavelengths of radiation and particles sizes were chosen, the Mie solution can be exactly calculated. At each small wavelength band, the model determined the intensity of the resultant scattered radiation in 1° increments, to determine the extinction coefficient, the scattering coefficient and the asymmetry parameter. The value determined for each broad radiation band was a simple arithmetic mean of the values for the 100 smaller radiation bands. Finally, the deliquescence effect was determined by setting up relative humidity boundaries from 80% to 99%, in 1% increments. No deliquescence growth is assumed for environmental relative humidities of 80% or lower. The end result of this code is the four output tables as described above. Because the Mie theory solution to this problem is exact, it only needs to be computed once. Therefore, the results of this subroutine are placed in a

look-up table within RAMS, to increase the speed at which the model can calculate the overall changes in τ, ω and g.

2.2.3 THE "OLD" RADCALC3 SUBROUTINE

Harrington (1997) wrote the current version of the radiation code for RAMS. The meat of this code lies in subroutine radcalc3 (see Figure 2.1). The code first determines the optical property values for optical thickness (τ), the single scatter albedo (ω) and the asymmetry parameter (g), due to cloud droplets and hydrometeors. Next, path lengths for water vapor, carbon dioxide and ozone (gases active in the Rayleigh scattering regime) are computed. Once this is complete, the code determines the downward solar fluxes and the Rayleigh scattering of this radiation caused by water vapor, carbon dioxide and ozone. Next, the blackbody fluxes are calculated over the five infrared bands, to give the two-stream results for all eight radiation bands. The three solar bands and the five infrared bands are treated separately, so that both longwave and shortwave heating rates

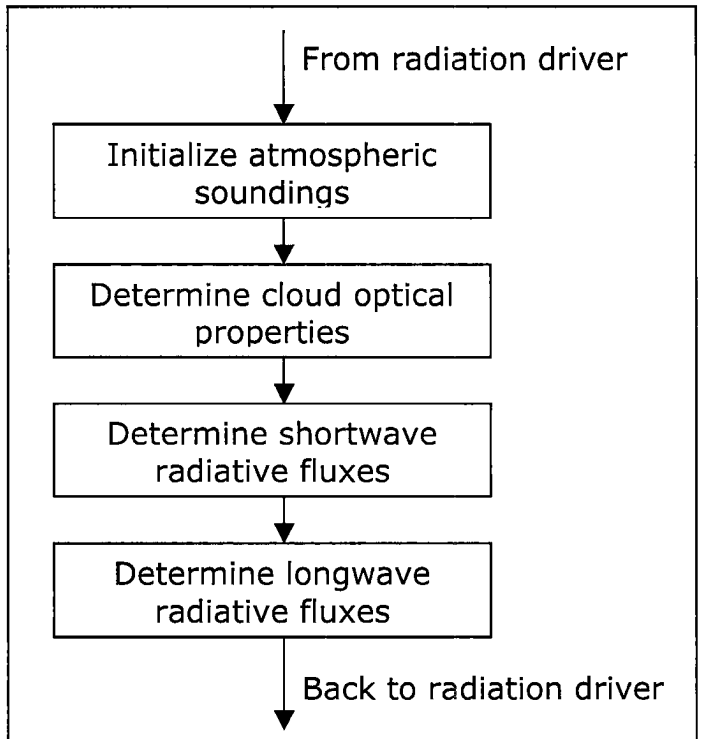

Figure 2.1: Flow chart of the original radiation scheme by Harrington (1997).

can be separately determined. This information is then passed back into the model for modification of the ice-liquid potential temperature, θ_{il}.

2.2.4 THE NEW AERORAD SUBROUTINE

Before discussing the new code, it is important to understand how aerosols are represented with in RAMS. As discussed previously, the aerosols are treated using a shell-core model. The remainder of the parameters describing aerosols are treated in an analogous manner to those describing hydrometeors. The number concentration of each aerosol species is assumed to be distributed log-normally, with a shape parameter of the distribution set at 1.8. The aerosols are also allowed to advect throughout the model. Finally, a number concentration and median radius of the distribution are both predicted for each aerosol species at each grid point. When the aerosol portion of the radiation subroutine is accessed (see Figure 2.2), through the radcalc3 subroutine, each aerosol category is treated separately, and these calculations are performed at each grid point. First, the total number concentration and median radius values are fed into a routine that creates a binned distribution of the aerosol. A look up table approach is used, where the percentage of the total concentration in each of the 17 bins was determined for 26 different median radii. A third order Lagrangian interpolation was used to determine the bin concentration for the given median radius. The binned concentrations were then fed into a subroutine that determines the total extinction and scattering, using the previously described look-up tables containing q_{ext}, q_{scat}, g_{asym} and the deliquescence growth factor. The amount of extinguished radiation, scattered radiation and forward-scattered radiation were determined based on binned aerosol concentrations of the aerosol in question and

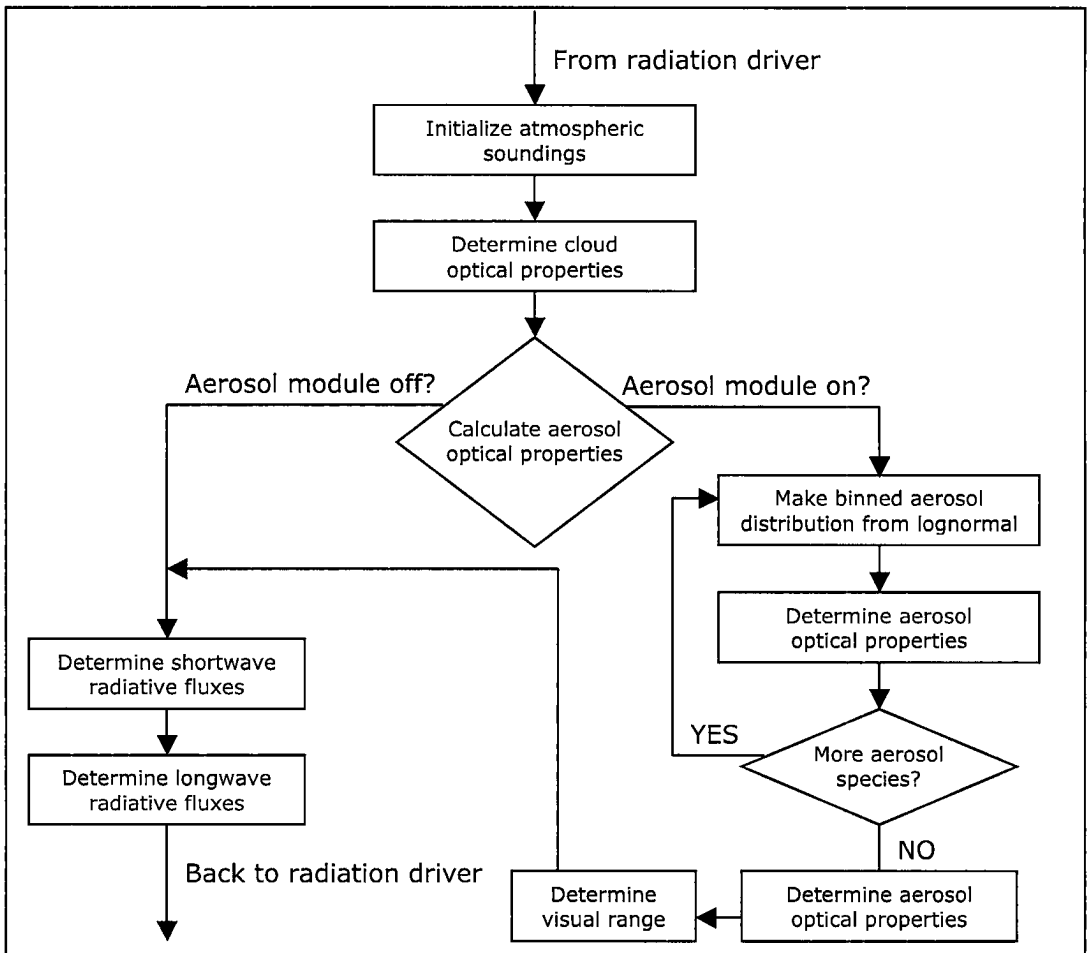

Figure 2.2: Flowchart of the new aerosol radiation scheme.

the relative humidity the aerosol were subject to. This process is then repeated until all active aerosols have been accounted for at which point the extinction and scattering values were summed together at each grid point. The summed values for the total extinction, total scattering and forward scattering were then added to their analog from the cloud droplets and hydrometeors. Slingo and Schrecker (1982) developed the method for determining the optical depth (τ), the single scatter albedo (ω) and the asymmetry parameter (g), from the values of scattering and extinction calculated from the aerosol subroutines, which are already weighted by a model-layer thickness:

g = total forward scattering/total scattering
ω = total scattering/total extinction
τ = total extinction

These values of τ, ω and g now contain information about the direct aerosol effect in the model, and are sent onward to the remainder of the radiation scheme.

Once the optical properties were combined to yield an overall value of the optical depth (τ), the single scatter albedo (ω) and the asymmetry parameter (g), a simple equation was used to determine visual range. The Koschmieder equation is simply:

$$x_v = 3.912 * b_{ext} / (dzl * 1000)$$

Where, b_{ext}/dzl is the optical thickness of the radiation band containing the visible spectrum, x_v is the visual range and both b_{ext} and x_v have the same length units (i.e., meters, kilometers, etc.). This equation was empirically determined, assuming that an "average" human eye can distinguish a contrast value of 2% (Seinfeld and Pandis, 1998). The visual range is a scalar value that is determined for each grid cell, and is not pathway dependent.

CHAPTER 3 –THE SAHARAN DUST EXPERIMENT

3.1 BACKGROUND ON THE SAHARAN DUST EXPERIMENT

The impact of atmospheric aerosols, as it relates to climate change, is still one of the most uncertain variables (International Panel on Climate Change, (IPCC), 2001). Dust aerosols are of particular importance, due not only to their scattering and absorption of solar radiation, but the perturbation they introduce in the terrestrial radiation spectrum (Tanre, et. al, 2003). The Saharan Dust Experiment (SHADE) was designed to experimentally determine parameters necessary to model the direct radiative forcing of Saharan dust. (Tanre, et. al, 2003) This was achieved by collecting concurrent measurements of radiances and irradiances together with physical and optical properties of atmospheric aerosols, in order to provide a radiative closure between *in situ* and remotely sensed data. The experiment was conducted under the auspices of the UK Meteorological Office, taking place between 19 and 29 September 2000 off the coast of Mauritania in and around the Cape Verde Islands.

3.2 SYNOPTIC WEATHER CONDITIONS DURING SHADE

The specific data used from the SHADE campaign for this study, was collected on the 24th and 25th of September 2000. These profiles were chosen due to the presence of the

Saharan dust layers, and that the structure of these profiles was each markedly different, in terms of the vertical distribution of dust concentrations. Both days were relatively cloud-free in the area of sampling, despite slight discolorations present in the METEOSAT satellite field (See figures 3.1 and 3.2). These discolorations are due to the presence of dust. There was no widespread airborne dust present on the 24th, but there were some small scale areas of dust, not easily seen on satellite (see figure 3.1). However, widespread dust was present and visible via satellite images on the 25th (see figure 3.2). Hurricane Isaac is located to the west of the sampling area, and had no

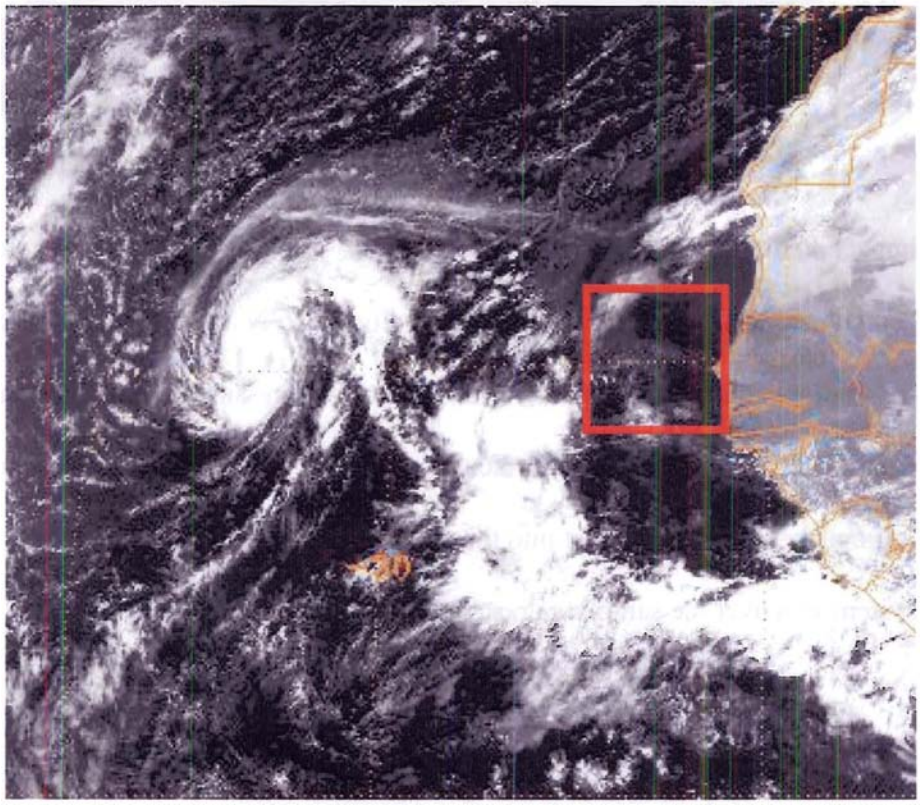

Figure 3.1: METEOSAT image off the western coast of Africa at 1130UTC, on 24 September 2000—red box is approximate location of sampling area.

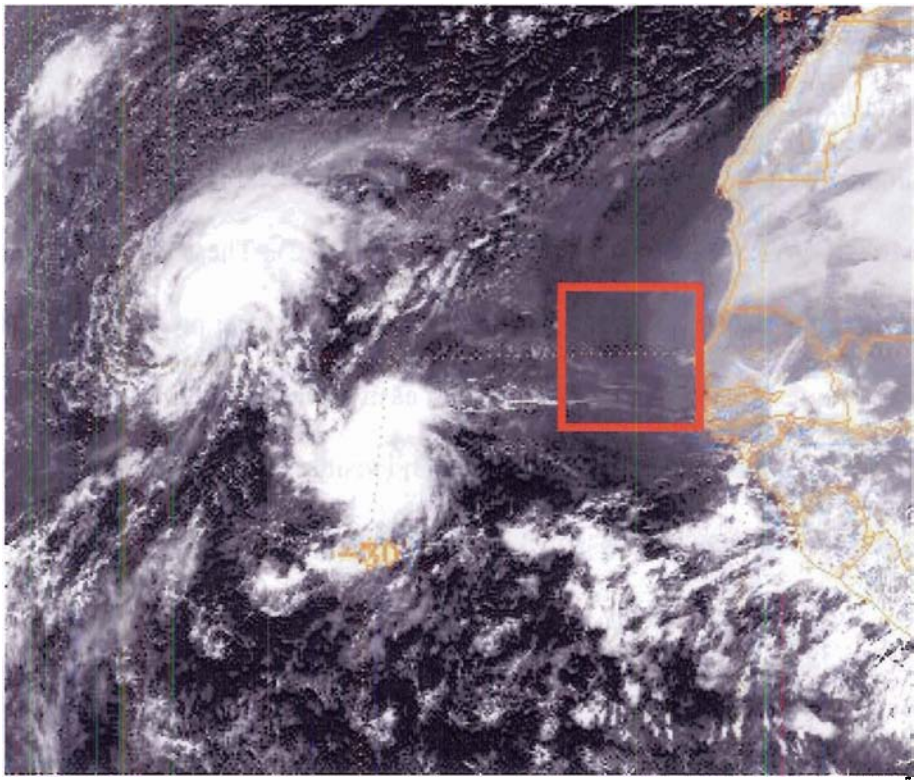

Figure 3.2: METEOSAT image off the western coast of Africa at 1130UTC, on 25 September 2000—red box is approximate location of sampling area.

impact on the sampling during these two days. The synoptic conditions were relatively benign near the sampling region (in the region of 15°N and 20°W) with little forcing present (see figures 3.3 and 3.4). However, a low-pressure circulation is present over the Sahara on the 24th generating surface winds, which were most likely responsible for lofting large amounts of dust into the atmosphere. The dust plume generated from this system was over the sampling area on the 25th.

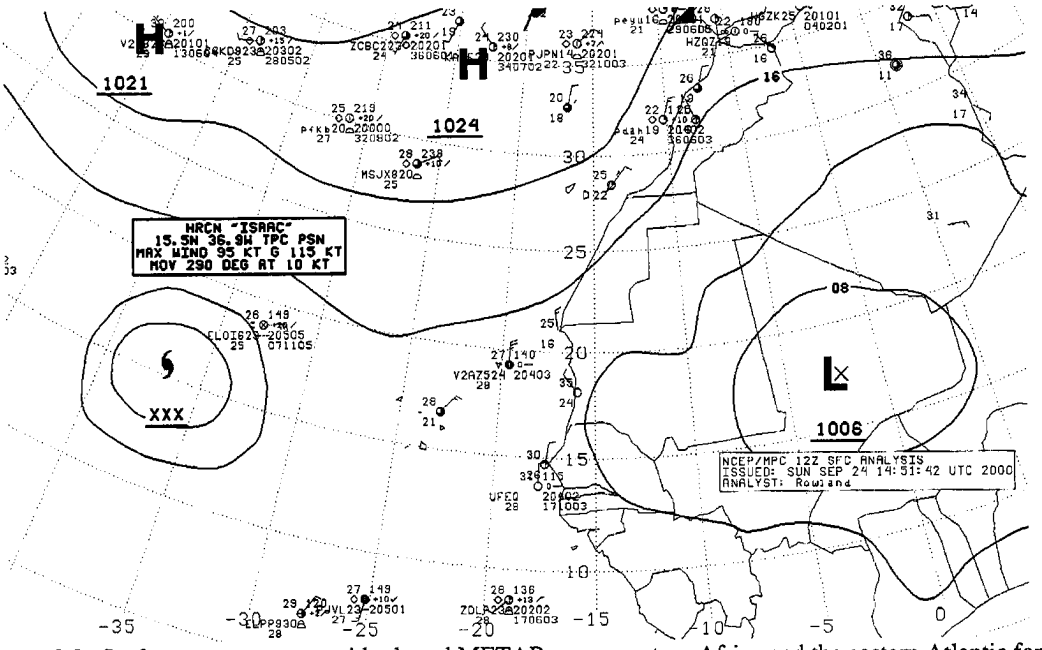

Figure 3.3: Surface pressure map, with plotted METARs over western Africa and the eastern Atlantic for 1200UTC on 24 September 2000.

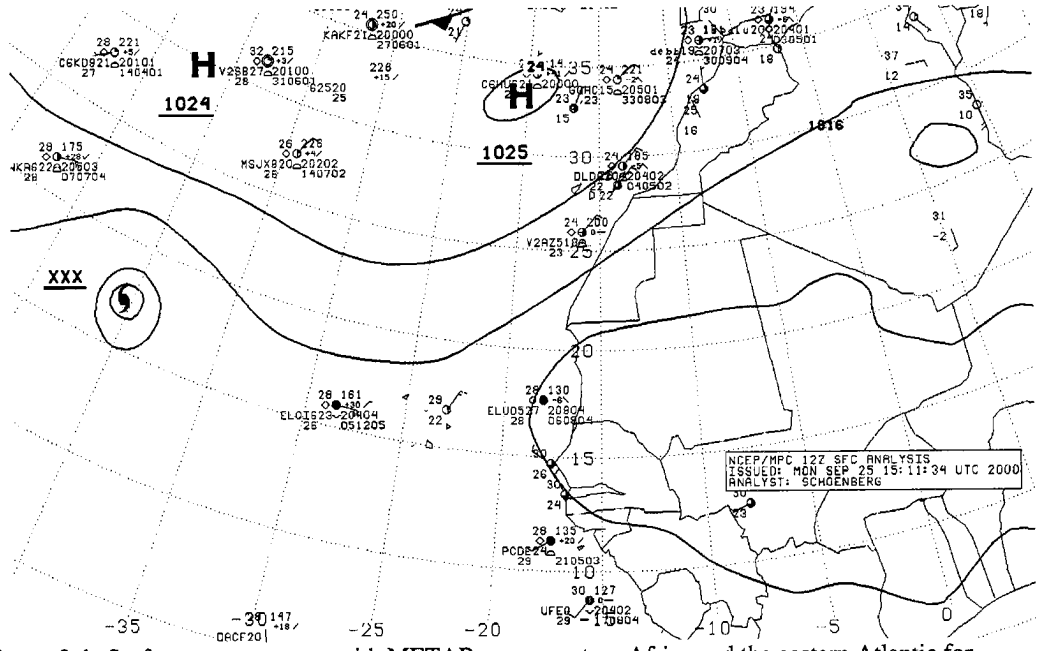

Figure 3.4: Surface pressure map, with METARs over western Africa and the eastern Atlantic for 12000UTC on 25 September 2000.

3.3 Relevant Instrumentation

All of the data used in this report, came from instrumentation aboard the UK Met Office's C-130 aircraft, described in Tanre, et. al 2003. Location of the aircraft was determined by a GPS transponder, while the meteorological conditions outside the aircraft were measured using a pressure probe, two temperature probes and two dew point/relative humidity probes. The size distribution of the aerosols was determined using a Passive Cavity Aerosol Spectrometer Probe 100X, (PCASP). Dropsondes were launched periodically throughout the flights of C-130, recording temperatures, dew points, and positional data using GPS transponders. These sondes were launched so that vertical moisture and temperature profiles could be obtained through different Saharan dust layers present during the SHADE campaign. A TSI 3563 nephelometer was used to determine aerosol scattering at three distinct wavelengths in the visible spectrum at 450nm, 550nm, and 700nm. Also on board the C-130 were two broadband radiometers, one facing upward measuring radiation in a band from 0.3 to 3.0μm, and one facing downward, measuring radiation from 0.7 to 3.0μm.

3.3.1 Dust Concentration Measurements

Throughout the SHADE campaign, the C-130 aircraft was operated on four different days dedicated to collecting data. The two specific days used for this study are the 24th and 25th of September, noted to have moderate and heavy dust loadings respectively. Each day's flight pattern consisted of three main types of legs: straight runs, low altitude orbits and profiles. For this study, three specific profiles were used, the first profile of the day

on the 24th, and two afternoon profiles on the 25th. All of the dust concentration data was collected using a Passive Cavity Aerosol Spectrometer Probe (PCASP).

During the entire campaign, the PCASP recorded the aerosol concentrations of 15 different bins ranging from 0.05μm to 1.5μm, at a time resolution of one second (Haywood, et. al, 2003). All of the aerosols counted using the PCASP were assumed to be mineral dust. For this study, the dust concentration data was averaged in 10-second groupings, as was the latitude, longitude and height data. Only the nine largest size bins were used to determine the aerosol concentration (from 0.15μm to 1.5μm), as the concentrations in the smaller bin were too noisy. After examining the PCASP data, the dust size distribution was assumed to be the sum of five lognormal distributions (Haywood, et. al, 2003). In order to be consistent with other ongoing avenues of RAMS research, the dust concentrations have only two modes. Since there is a mismatch in the number of assumed lognormal modes of the dust concentrations, a method was developed to match the five-mode information from Haywood, et. al (2003) to a two-mode

SHADE DUST PARAMETERS

	# Fraction	r_m, μm	σ
Mode 1	70.30%	0.04	1.6
Mode 2	19.50%	0.11	1.3
Mode 3	7.70%	0.30	1.6
Mode 4	2.00%	1.07	1.3
Mode 5	0.50%	1.80	1.5

FITTED PARAMETERS FOR RAMS

	# Fraction	r_m, μm	σ
Mode 1	94.30%	0.056	1.8
Mode 2	5.70%	0.690	1.8

Table 3.1: Parameters for five-mode dust representation of Haywood, et. al (2003), along with the best fit parameters determined for RAMS.

representation to be used in this study (see table 3.1). The parameters for the two-mode representation were determined by minimizing an error cost function

$$\text{Cost function} = \Sigma(([\text{five-mode}] - [\text{two-mode}])^2 * r_{bin}{}^2)$$

The error cost function is a function of the relative sizes of the two peaks, as well as their median radii. For each cost function, bins were set up from 0.5nm to 4μm, with a bin-width of 0.5nm. At each bin, the square of the difference in concentrations of the estimated five-mode dust distribution and the assumed two-mode distribution, were multiplied by the radius squared—since particle extinction is a strong function of cross-sectional area. The sum of these errors from 0.5nm to 4um constituted the total cost function. The minimization of the cost function yielded a two-mode distribution as pictured in Figure 3.5, with the five-mode distribution picture for reference. Once the two-mode distribution was determined, the sum of the concentrations of the nine bins from the PCASP were then extrapolated to the entire size domain, to determine an overall concentration value to be used in the model.

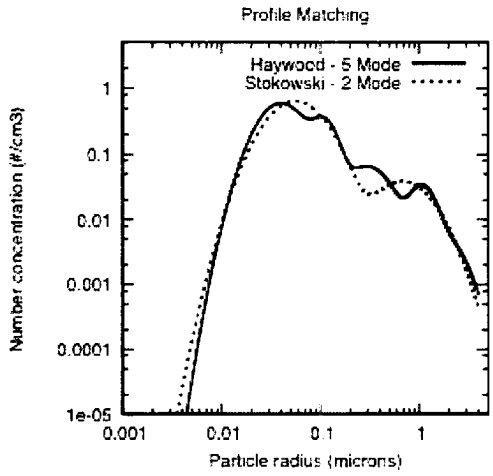

Figure 3.5: Size distributions for the five-mode dust profiles from Haywood, et. al (2003) and from this study.

There were three dust profiles (see figure 3.6) that were used in this study, one from the initial ascent of the C-130 on 24 September 2000 (profile 1), and two afternoon profiles

on 25 September 2000 (profiles 2 and 3). Each of these profiles exhibits different magnitudes and locations of the dust concentration maxima. Profile 1, shows a maximum around the level of the marine boundary layer top (800m), with elevated concentrations (300-600/cm^3) in the 3000-4800m range. The second profile shows a small maximum around 1800m, and a much more highly concentrated dust (~1200/cm^3) in the 2500-4500m layer. Profile 3 shows a strong maximum (~3800/cm^3) just above marine boundary layer top (800-1600m), and again contains elevated concentrations above 3000m (600-1200/cm^3). Each of these profiles is markedly different, and according to Haywood, et. al (2003), the height location of each maxima indicates a different source region within the Sahara, as determined by back trajectory analysis.

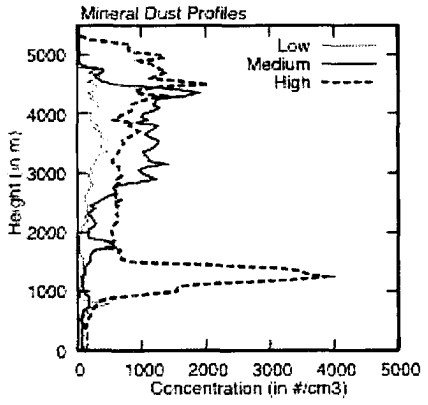

Figure 3.6: The three dust concentration profiles used in this study.

3.3.2 Dropsonde Measurements

Throughout the measurement campaign, dropsondes were launched to record temperature, moisture and wind profiles at various locations. For this study, the dropsonde most closely located in time and space to the given dust profile was used in comparison to the model results (Table 3.2). All three profiles showed good temporal co-locations (within 25 minutes of the end of a given vertical profile), but the spatial co-locations varied greatly. For the first profile, there was very good spatial co-location,

while the second profile had moderately good co-location. Unfortunately, there was not a particularly good spatial co-location for the third profile.

Profile #	Date	Time (UTC)	Location (Avg)	Dropsonde Point
1	9/24	1012-1037	16.78°N, 22.75°W	16.83°N, 22.49°W, 1050UTC
2	9/25	1501-1518	16.02°N, 21.02°W	15.67°N, 20.04°W, 1535UTC
3	9/25	1729-1745	15.11°N, 18.46°W	15.85°N, 20.45°W, 1810UTC

Table 3.2: Average spatial and temporal locations of the three dust profiles, along with the closest corresponding dropsonde.

3.3.3 Radiation Measurements

Many different types of radiation measurements were taken during the SHADE campaign. For irradiance measurements in the shortwave, a total of four Eppley broadband radiometers were placed on the C-130 aircraft. Both the upward and downward facing setups contained one radiometer measuring the 0.3-3.0μm broadband with a clear dome, and one measuring the 0.7-3.0μm broadband with a red dome (Haywood, et. al, 2003). The longwave irradiance measurements were collected using upward and downward facing pyrgeometers covering a broadband of radiation from 3-50μm (Highwood, et. al, 2003). Data from the TSI 3563 nephelometer recorded the amount of radiation scattered at 450nm, 500nm and 700nm (Haywood, et. al, 2003). Since the most intense radiation incident on the Earth is near 550nm, that specific channel will be used for comparison to modeled values of extinction and hence will be a check on the modeled visual range. Finally, the SHADE campaign also recorded absorption at 567nm using a Radiance Research Particle Soot Absorption Photometer (PSAP). This was used to determine the imaginary refractive index of mineral dust.

CHAPTER 4 –THE MODEL

4.1 MODEL INITIALIZATION

The recently modified version of the Regional Atmospheric Modeling System (RAMS) was used in this study. Three sets of model runs were completed, one set for each of the three mineral dust concentration profiles used from the SaHAran Dust Experiment (SHADE). There were eight model runs in each set corresponding to a binary matrix of on/off switches for each of the three aerosol species considered. The following describes how the model was initialized for this particular study.

4.1.1 GENERAL MODEL INFORMATION

The model runs that were completed for this study were done using a single grid in large eddy simulation (LES) mode with two spatial dimensions, an east-west horizontal dimension and a vertical dimension, centered at 15°N, and 20°W. The grid-spacing was 100m in the horizontal, with a variable spacing in the vertical—50m in the lower 5km of the domain (so that the aerosol distribution could be well-resolved), and then stretching by a factor of 1.1 up to the model domain top (~23.2km). There were 100 horizontal grid points and 138 vertical grid points. The model was initialized at 1200UTC on the day that the dust profile was collected (either the 24th or the 25th of September 2000).

The model was allowed to run for 78 hours, with a timestep of 2 seconds. The lateral (east-west) boundary condition was cyclic, with no motion allowed in the north-south direction. The Coriolis force was not included, as the model domain was at low latitude and contained only an east-west horizontal dimension. The Harrington (1997) radiation scheme was used, with radiative updates being performed every minute. The Deardorff (1980) TKE eddy diffusion scheme was used, since the model was being run as an LES model.

The model was initialized in a horizontally homogeneous fashion, with temperature, moisture and wind profiles given by NCEP reanalysis at the grid point closest to the profile in question (figure 4.1). No perturbations to the wind or temperature field were prescribed. The surface was assumed to be ocean, with an sea surface temperature (SST) also derived from the closest NCEP reanalysis grid point. Level 3 microphysics was used, with all of the hydrometeor species having prognostic calculations performed to determine their concentrations. The concentrations of cloud condensation nuclei (CCN), giant cloud condensation nuclei (GCCN) and ice-forming nuclei (IFN) were prescribed, and were initialized in a horizontally homogeneous fashion.

Profile #	Date	Time (UTC)	Location (Avg)	NCEP Reanalysis Point
1	9/25	1501-1518	16.02°N, 21.02°W	15.0°N, 20.0°W, 1200UTC
2	9/24	1012-1037	16.78°N, 22.75°W	17.5°N, 22.5°W, 1200UTC
3	9/25	1729-1745	15.11°N, 18.46°W	15.0°N, 17.5°W, 1200UTC

Table 4.1: Spatial and temporal locations of the three dust profiles used in this study, along with the NCEP reanalysis data points used for model initialization.

4.1.2 Physical Characteristics of Aerosols

The main purpose of this study was to allow ammonium sulfate, sea salt and mineral dust to be radiatively active within the model. They are not all, however, new independent variables, as CCN is used as a proxy for ammonium sulfate particles, and GCCN was used as a proxy for sea salt particles. Therefore any changes to the concentrations of these species need to be looked at carefully, as they come with a corresponding change in the number of CCN or GCCN available for the microphysics package. The initial vertical distribution of CCN (ammonium sulfate) is pictured in figure 4.1a. The initial surface concentration was assumed to be 300/cm^3, with an e-folding height of 2.5km. After decaying up to 5km, the concentration is assumed to hit a background concentration, which is present throughout the remaining depth of the model (at 40.6/cm^3), and decreases to zero in the top six vertical layers. For CCN, a 40nm median radius was assumed for its size

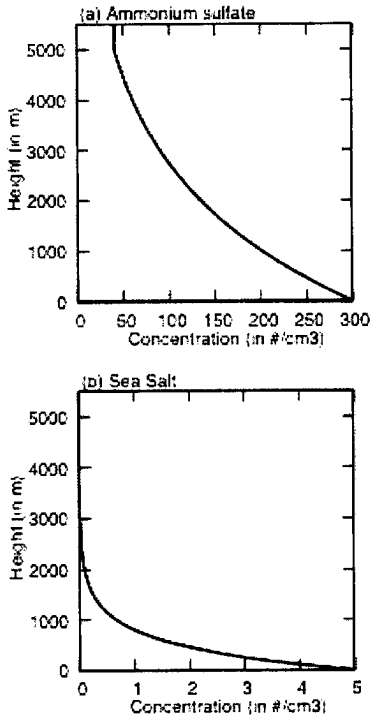

Figure 4.1: Initial vertical profiles of (a) ammonium sulfate, and (b) sea salt.

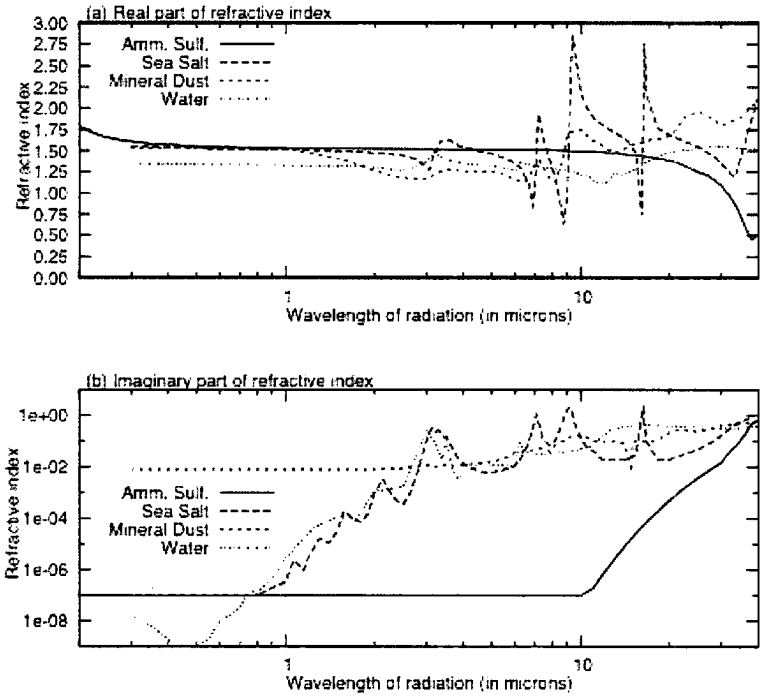

Figure 4.2: Real (a) and imaginary (b) parts of the refractive index for the four species present in the aerosols modeled in RAMS.

distribution. A similar model is used for the concentration of sea salt (figure 4.1b). Following the idealized observed GCCN profile of Van den Heever, et. al (2005), a beginning surface concentration of GCCN (sea salt) was assumed to be $5/cm^3$ with a median radius assumed to be 0.3μm. Because the median radius was much larger than for the CCN, the e-folding height of sea salt was assumed to be 500m. Again after decaying up to 5km, the concentration was assumed to hit a background state for the remainder of the depth of the troposphere ($4.54 \times 10^{-5}/cm^3$), again decreasing to zero at the model top.

Because the backbone of the new aerosol radiative model is based on Mie theory, figure 4.2 shows the wavelength dependence of both the real and imaginary parts of the refractive index:

$$m = n + ik \qquad \text{(Eq. 4.1)}$$

where m is the total refractive index containing information about the ability of a species to refract (n) and to absorb (ik) radiation. In the visible range, where the bulk (~70%) of the energy exists, the real part of the refractive index is relatively constant but then varies dramatically when the wavelengths of radiation become infrared. As for the imaginary part of the refractive index—in the visible range, only mineral dust has any significant absorbing power, with values of 5 to 6 orders of magnitude greater than all other aerosol constituents. This gap closes, and all aerosol constituents are within an order of magnitude at the highest modeled wavelengths.

4.1.3 Model Run Identification

For each set of initialization conditions, eight model runs were performed, by varying which atmospheric aerosols were radiatively active in the model. Each model run was given an identification number using the following format:

MMDD_RASM

Where MM is the two-digit month of the simulation (always 09); DD is the two-digit date of the simulation (24 or 25); R is a binary value (0 – off, 1 – on) explaining whether the radiation module is active and A,S, and M are binary values explaining whether the ammonium sulfate, sea salt and mineral dust (respectively) are radiatively active in the model. When R was set to zero, M had a value of 1 or 2 denoting which dust concentration profile was used on a given day. For the second profile on the 25th, the

binary-on value was set to 2 for A, S and M. For example, 0925_1220 refers to the second model run on the 25th of September, with the radiation module active, and both ammonium sulfate and sea salt as radiatively active aerosol species.

4.2 Results from Profile 1 – 25 September 2000

For this set (and every subsequent set) of model runs, the analysis of the model output will be confined to four main areas: changes in the temperature profile; changes in the radiation profiles, changes to the vertical velocity profiles, and a discussion about the modeled visibility. This specific case will be covered in much greater detail than the remaining model runs, due to the fact that this set of runs was the baseline for the sensitivity discussion in Chapter 5. For all subsequent sets of model runs, pertinent details will be discussed, with similar results being highlighted and not discussed in great detail. All of the data presented will be horizontally averaged, excluding the outermost two grid points on either horizontal extent of the domain, using 96 values.

This set of model runs was completed with the common thread being the initial conditions that were related to the mineral dust profile collected by the SHADE C-130 aircraft from 1501-1518UTC on the 25th of September 2005. The dust profile collected during this phase of the collection process is illustrated in figure 4.3. The main features of

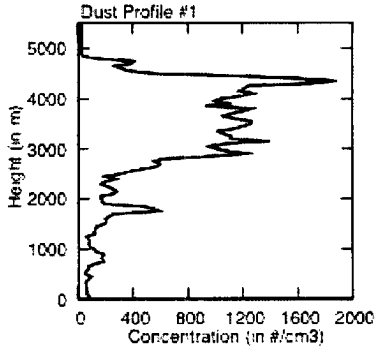

Figure 4.3: Vertical concentration profile for dust profile #1.

this dust layer are highly elevated dust concentrations in the 3,000 – 4,500m range, with strong local maxima at 1,750m and ~4,350m. The dust concentration averaged between 1,000 and 1,200 particles/cm^3 in the dusty layer, with a profile maximum of 1,889 particles/cm^3. Using this dust profile and the associated NCEP initialization point (see figure 4.1), the following discussion highlights the differences caused by the radiative interaction of each of the three aerosol species.

4.2.1 Changes in the Temperature Profile

Temperature and moisture profiles are presented for each of the eight model runs in this data set (Figure 4.4). Times chosen for this analysis were the initial time (12UTC), and

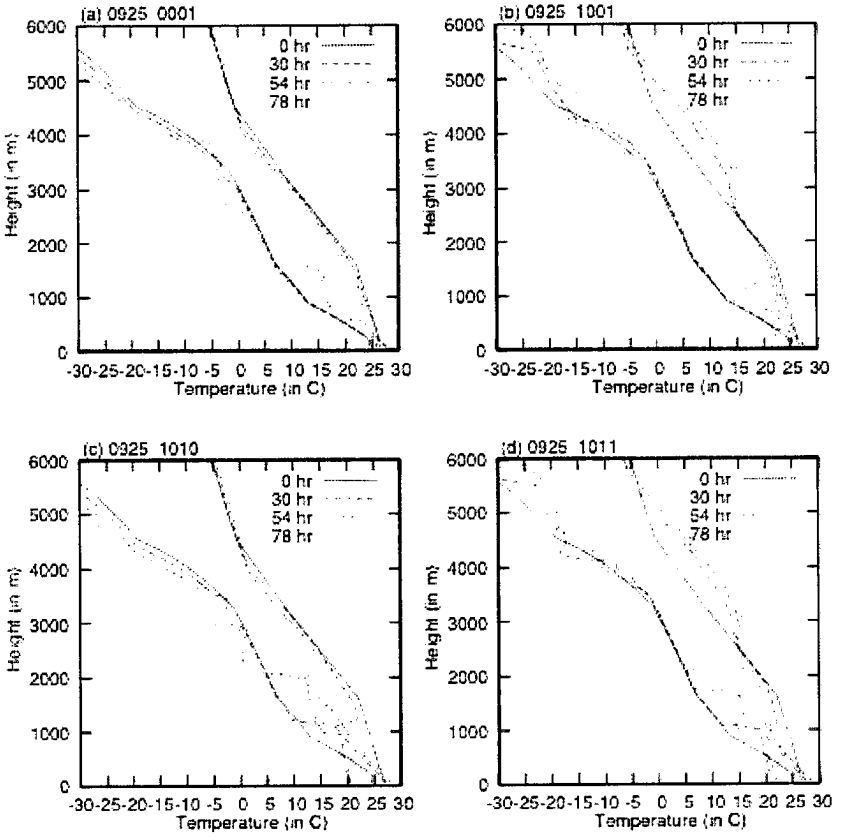

Figure 4.4 (panels a-d): Temperature and dew point profiles for model runs from the 0925_0001 family.

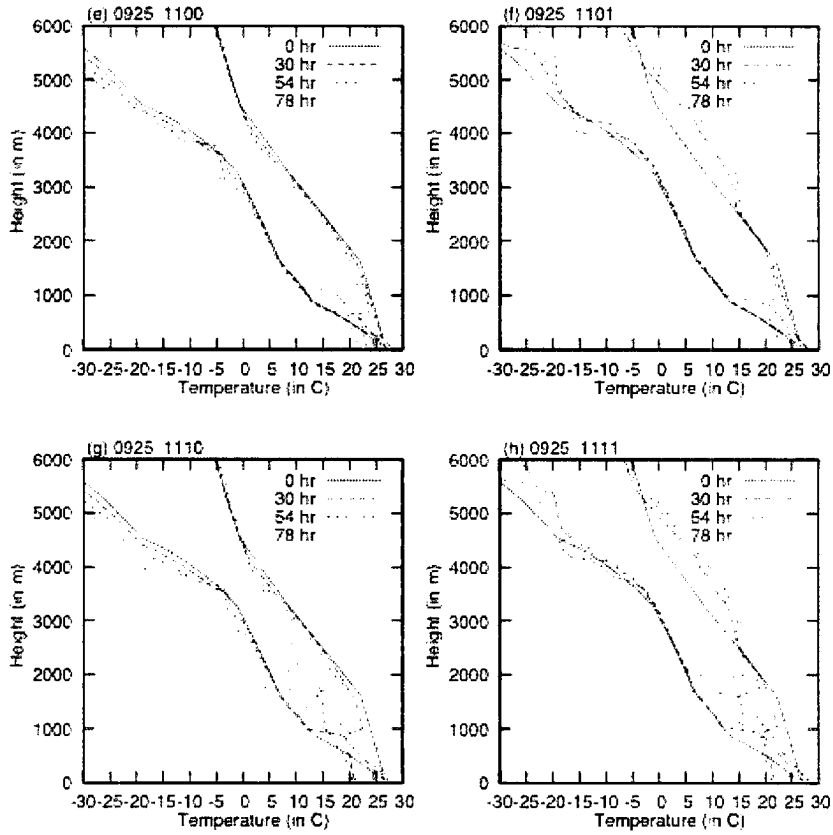

Figure 4.4 (panels e-h): Temperature and dew point profiles for model runs from the 0925_0001 family.

18UTC for the next three days, representing 30, 54 and 78 hours of model simulation time respectively, so that successive daytime solar heating events could be tracked.

There are a few things worth noting as it relates to the temperature profile for the no active aerosol case (0925_0001, figure 4.4, panel (a)). From the initial sounding, the temperature decreases slightly throughout the lower 4,000m of the model domain. Figure 4.4 only shows the temperature field below 6,000m, because there was essentially no change in temperature field with time above that level. Only very subtle changes occur to the moisture profile below 3,000m, with a general drying of the layers above that. An interesting feature to note is the development of a temperature inversion/moist layer that

grows in height with time. By the end of the model run (78 hours), the cloud base is at 1,600m. This value is quite high, and is rather unreasonable for the height of a marine boundary layer. This issue will be addressed in the sensitivity study in Chapter 5, with the results here taken as is, with the understanding that there is a lack of realism presented by these results.

Radiatively active aerosols within the model bring changes in the temperature and moisture profiles—some are subtle, others are hard to miss (figure 4.4, panels b-h). When looking at the effects of ammonium sulfate, there is only one readily apparent effect—it seems to keep the boundary layer from growing. In all four cases where ammonium sulfate is active, the temperature and moisture inversion is lower than during

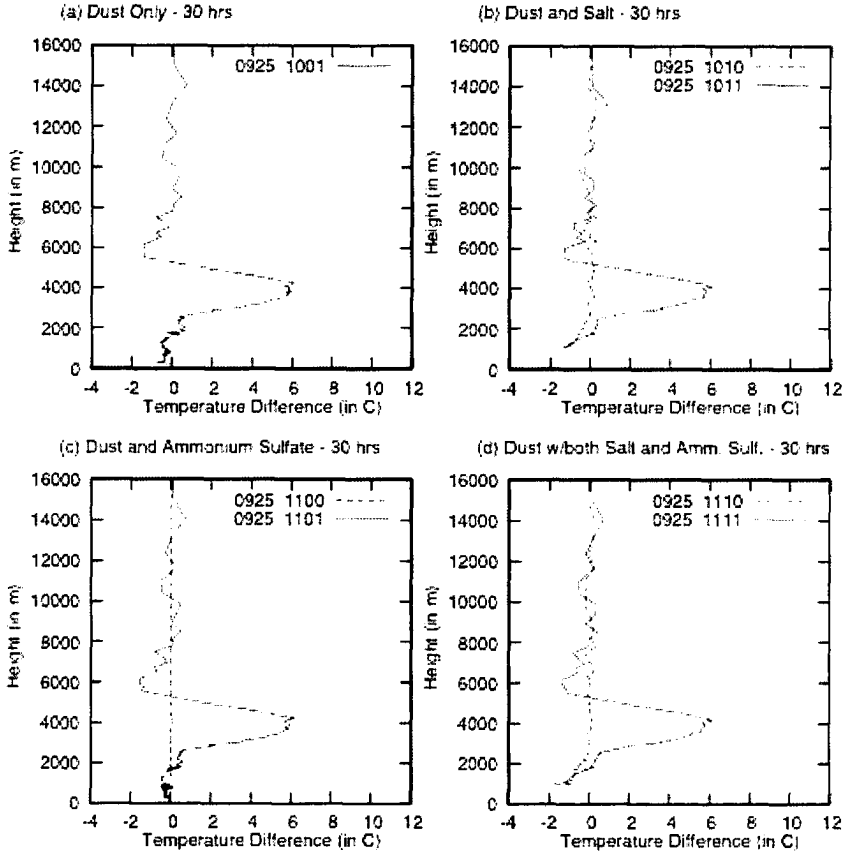

Figure 4.5: Temperature differences for all of the aerosol runs compared to the no aerosol run at 30 hours.

the corresponding runs without ammonium sulfate. Aside from that, there is very little to speak of as an ammonium sulfate effect on either temperature or moisture. Nearly the same thing can be said of sea salt, but with one major difference—in all four runs containing the sea salt radiative effect, the inversion layer is markedly higher than corresponding runs without sea salt as radiatively active. Again, there are very small, if any, noticeable temperature and/or dew point profile changes as a result of having sea salt radiatively active.

There are two effects from the radiative activity of mineral dust that are apparent in figure 4.4. The first is that the mineral dust, in general, suppressed the growth of the

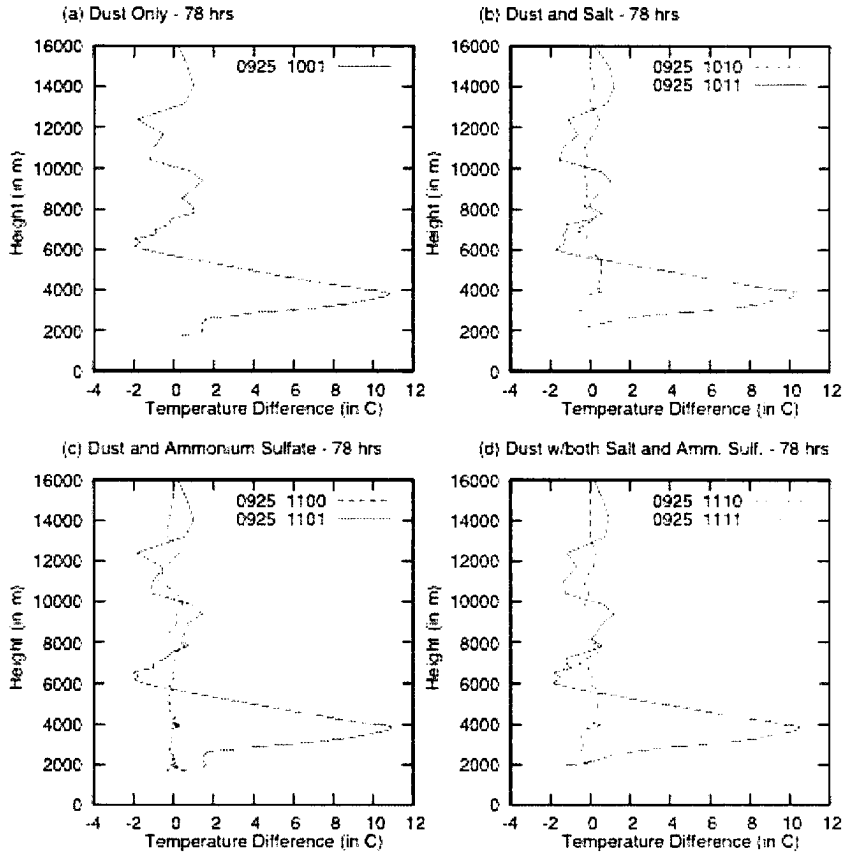

Figure 4.6: Temperature differences for all of the aerosol runs compared to the no aerosol run at 78 hours.

mixed layer. However, the main aerosol effect that is seen through the temperature field is the dramatic heating in the highly concentrated dust layer. The magnitude of this effect with time can be seen in figures 4.5 and 4.6. After 30 hours of simulation time (two daytime periods), a maximum heating of 6°C is seen at 4,000m, and at 78 hours, the difference from the run with no radiatively active aerosols is over 10°C. Again using figures 4.5 and 4.6, small changes in the temperature profile are observed with the other two aerosol species, but nothing as pronounced as is seen when the dust layer is present. In general, the inversion layer is also suppressed by the presence radiative presence of mineral dust.

4.2.2 Changes in the Radiation Streams

In order for the previously described temperature changes to occur, changes must also have been made to the radiation streams within the model. Because the changes to the radiation streams are immediate, the magnitudes of the irradiances will be shown for only two times, the initial time (12UTC) during nearly overhead sunlight, and 12 hours later (00UTC), with no sunlight present. As previously stated the model contains three solar bands with modeled wavelengths from 245nm to 4.64μm and five infrared bands ranging from 4.64μm to 40μm. Figure 4.7 shows the simulated upward and downward irradiances for both the shortwave and longwave radiation in the model at 12UTC for all eight different aerosol representations. Again, there are a few subtle differences in the eight different panels on figure 4.7. There is no discernable change to the radiation field caused by the presence of ammonium sulfate. Only one subtle change is evident with the radiative treatment of sea-salt—a slight increase in downwelling longwave radiation near

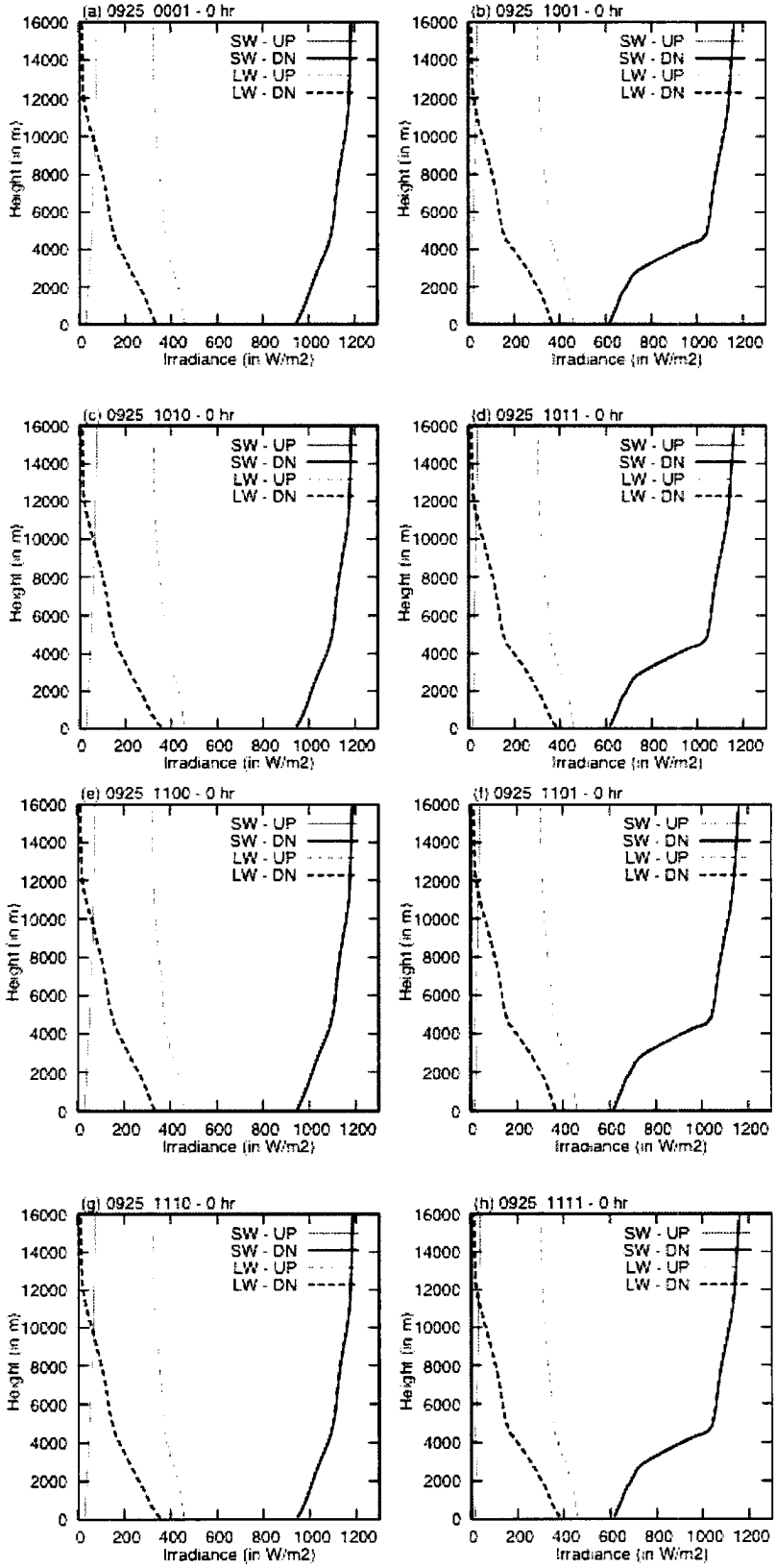

Figure 4.7: Initial short- and longwave radiation streams for model run 0925_0001 and family.

the surface. The most obvious changes to the modeled irradiances are manifested with the presence of mineral dust. Downwelling solar radiation is dramatically reduced to a surface irradiance value of 618 W/m^2 from 947 W/m^2 when dust is not present.

The change in nighttime radiation streams due to the radiative activity of aerosols is much less drastic than the effect during the daytime (figure 4.8). Again ammonium sulfate causes no immediately discernable changes in the radiation streams. The sea salt however causes one large change—a drastic and sudden increase in downwelling longwave radiation at 300m (e.g., figure 4.8, panel c). This change is indicative of the formation of a low-level cloud. The presence of mineral dust does cause an increase in

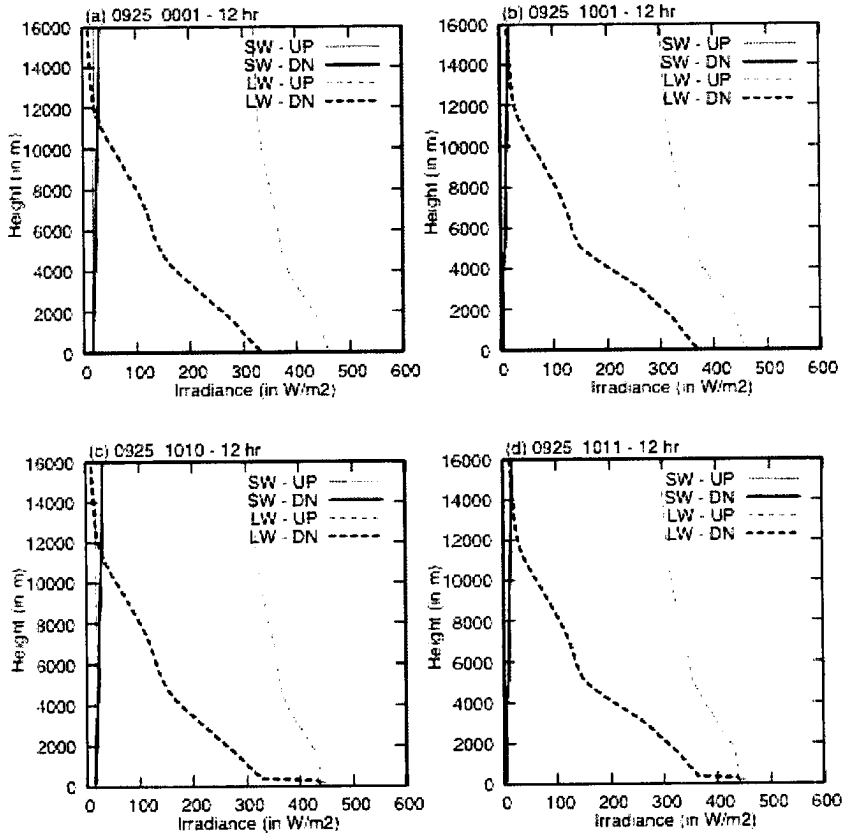

Figure 4.8 (panels a-d): Short- and longwave radiation streams for model runs containing the 0925_0001 family after 12 hours of simulation time.

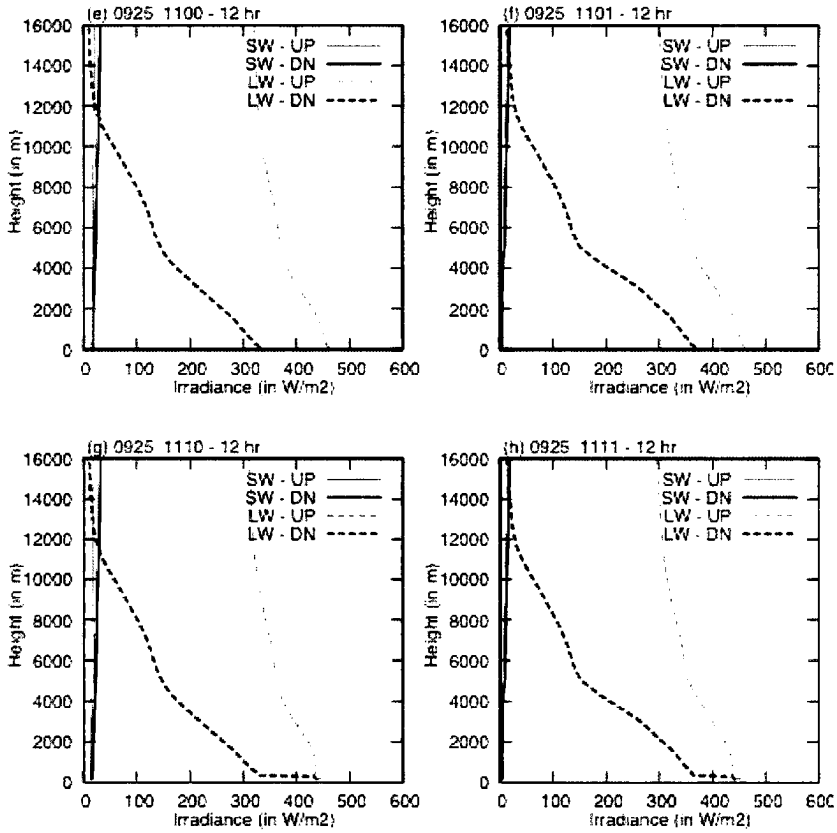

Figure 4.8 (panels e-h): Short- and longwave radiation streams for model runs containing the 0925_0001 family after 12 hours of simulation time.

downwelling longwave as well (e.g., figure 4.8, panel b), but this originates higher up in the atmosphere than the change associated with sea salt. This is due to large amounts of heating present in the layer, and is therefore accompanied by a corresponding increased blackbody irradiance.

While this qualitative analysis yields trends, it is important to quantify the changes in the radiation streams so that a full picture of the direct radiative effect can be determined. As far as the issue of cloud contamination, if cloud has formed in a field whose analysis is desired, the analysis will only be done above the low-level cloud layer, as no upwelling fields were analyzed when cloud contamination existed. It should be noted that the

formation of a cloudy layer was determined solely radiatively, i.e., only if a sharp low-level increase in downwelling longwave radiation was present.

In examining the upwelling radiation streams of both longwave and shortwave radiation, the same qualitative features exist in both plots (Figure 4.9). Ammonium sulfate yields essentially zero change in both the upwelling short- and longwave radiation streams. The sea salt does show the ability to decrease both upward bound radiation streams, although only slightly (0.75W/m^2 longwave, 3.0W/m^2 shortwave). As is expected the major changes to the upwelling radiation streams are due to the presence of mineral dust. In the shortwave, the decrease in upwelling surface radiation is due to lower downwelling shortwave radiation values and hence the surface has less radiation to reflect upward. The continuing decrease in upwelling shortwave radiation is due to the strongly absorbing nature of the mineral dust, and it presence throughout the depth of the model domain. The overall effect of the mineral dust is to reduce outgoing shortwave radiation at the top of the model domain (22.3km) by 41.3W/m^2. Mineral dust does have the same effect in the longwave as the shortwave, reduction in upwelling radiation. This is again due to the absorbing nature of the mineral dust, coupled with its high concentration in the 3,000m to 4,500m layer. The

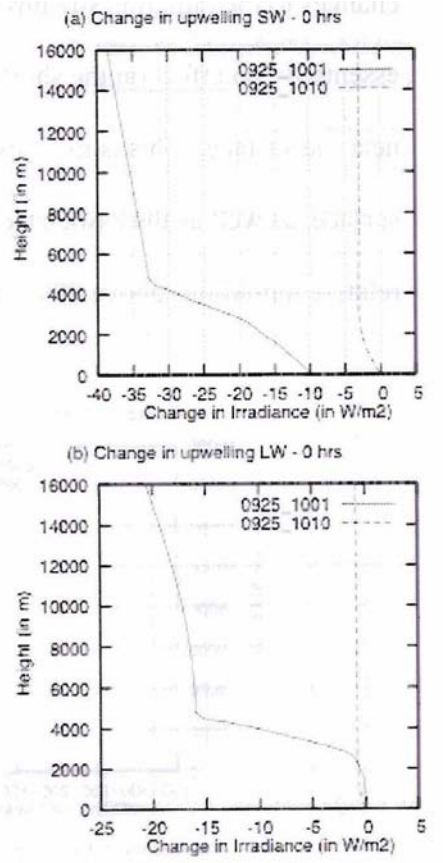

Figure 4.9: Change in irradiance of upward short- and longwave radiation streams for profile 1 due to sea salt and mineral dust

trapping effect of mineral dust in the longwave at the top of the model domain is equal to 24.8W/m^2, for a total reduction of outgoing radiation of 66.1W/m^2.

The effect of the aerosol species is much more dramatic when looking at downwelling streams (figure 4.10). As with all previous discussions, ammonium sulfate offered no changes to the radiation streams (under 1.0W/m^2 at any given level). Sea salt had essentially no effect on the shortwave, but did have a strong local effect in the longwave, near the surface. This is most likely due to the large mass of the sea salt particles near the surface, as well as the associated liquid water that deliquesces on sea salt particles at relative humidities above 80%. Unfortunately, this effect could not be tracked at later

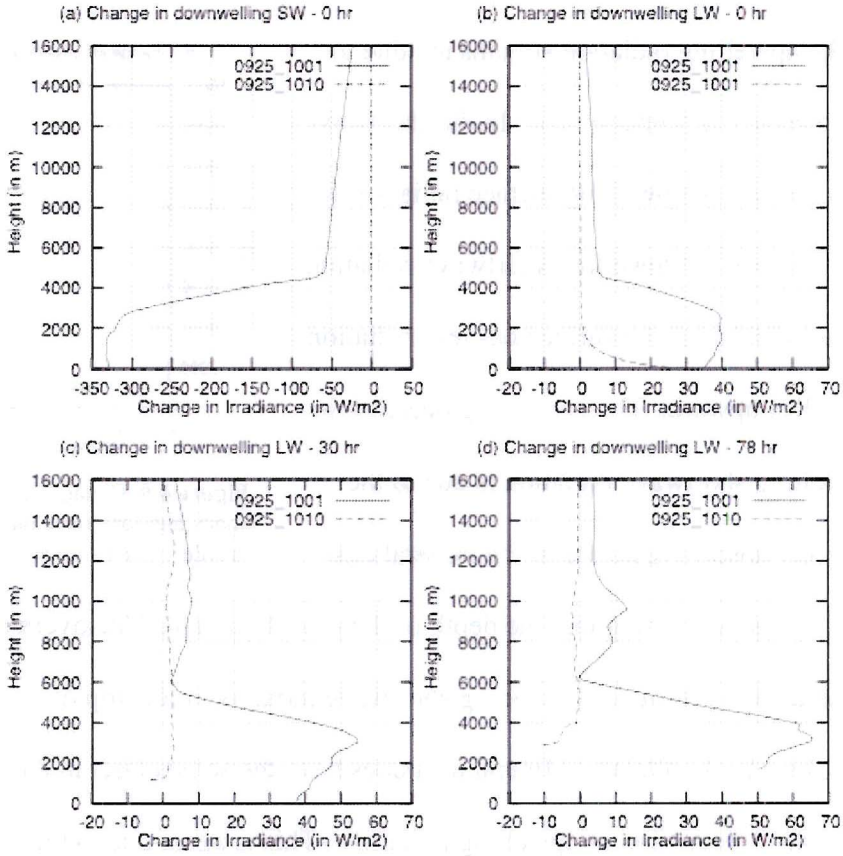

Figure 4.10: Change in irradiance of downward short- and longwave radiation streams for using profile 1 due to sea salt and mineral dust, after various simulation times.

times due to the presence of clouds in the field during the sea salt model runs. The mineral dust radiative effect, however, was quite strong. In the longwave, there was an increase in the amount of downwelling radiation present, beginning in the dusty layer and progressing downward. This is due two complimentary effects; first the mass of the mineral dust will emit in the longwave just by its presence, second is the heating that was taking place in the dusty layer. The increase at the surface was $35W/m^2$. This value pales in magnitude to the modeled direct radiative effect (reduction of downward shortwave irradiance) of mineral dust at $328W/m^2$. This direct radiative effect value is much higher than anticipated, when compared to the maximum instantaneous values determined during the SHADE campaign of approximately $129 \pm 5W/m^2$ (Haywood, et. al, 2003). Their value of $129W/m^2$ was determined only after adjusting the input values of the imaginary part of the refractive index from their original data set. Due to the initial mismatch of the direct radiative effect, sensitivity studies were performed varying the imaginary part of the refractive index; these results will be presented and discussed in chapter 5.

4.2.3 Changes in the Maximum Vertical Velocity Profile

It has been postulated that a decrease in surface bound solar energy would reduce turbulent motions in the planetary boundary layer (Miller, et. al, 2004). An investigation into this effect was initiated within the confines of these model runs. Initially, the vertical momentum flux (w'^2) was looked at, but since the overall vertical motions within the model domain were in the 10^{-5}m/s range, the focus of the investigation changed to the

maximum vertical velocity profile. The maximum vertical velocity fields for model runs containing ammonium sulfate again showed essentially no change, despite having the general effect of suppressing growth of the boundary layer (as determined by the previous discussion on temperature profiles). Sea salt also showed no changes to the field after small periods of time, but since cloud contamination was present after a short period of time, the maximum vertical velocity profiles are not directly comparable to the run containing no aerosols. An interesting feature however is present in the data from the mineral dust runs (see figure 4.11). During the daytime comparisons (6hr and 30hr modeled time, 1800UTC), the maximum vertical velocity for the dust-laden case was positive, whereas the no aerosol run had a completely subsiding vertical velocity profile. The initial thought is that this could be due to instantaneous heating where dust is present, causing very small-scale upward vertical motion due to buoyant effects. Without a manner to look at the turbulent field accurately, this can only be an assertion. It is also interesting to note that overnight the profile switches to a completely subsiding profile in the mineral dust case, with higher magnitudes of the minimum downward velocity when compared to the no aerosol case.

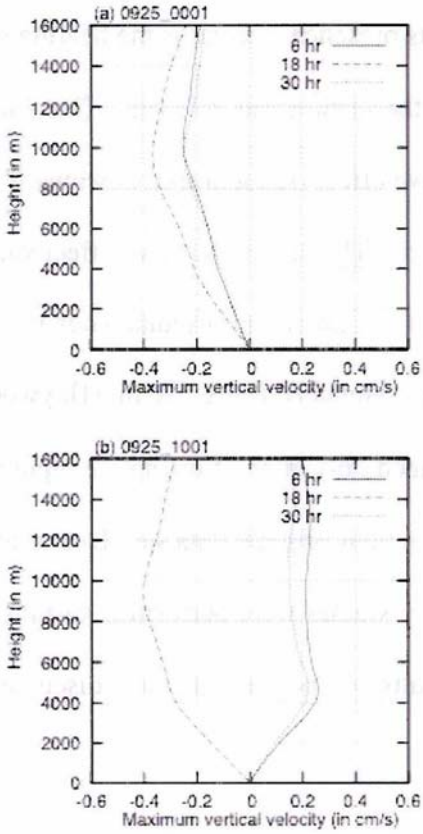

Figure 4.11: Maximum vertical velocity profiles for profile 1 cases containing no aerosols (a) and dust only (b).

4.2.4 Investigation into Visibility

As previously stated the prediction of visibility due to the presence of aerosols has great importance to military operations in areas such as Iraq and Afghanistan. This new variable is going through its initial testing to determine if it is behaving properly. Since the ammonium sulfate aerosol has negligible contributions to visibility degradation in this model, the investigation will be confined to mineral dust and sea salt. Figure 4.12 shows the modeled visibilities of only dust, and dust in combination with sea salt at three different times. There are two main points to notice in the dust only run (figure 4.12, panel a). First the visibility field gets smoothed out with time, most likely due to diffusion effects. Second, the low visibility caused by the dusty layer reaches higher altitudes with time and is most likely attributed to the previously mentioned buoyant transport. The only difference between the dust only run and the dust with sea salt run is that the surface visibility is much lower when sea salt is included. This is due to the scattering caused by the deliquesced water onto the already quite large sea salt

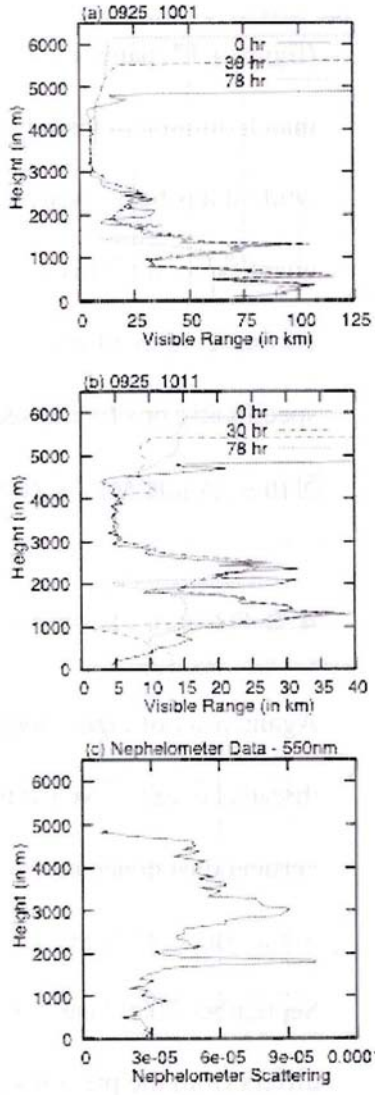

Figure 4.12: Modeled visible range values for profile 1 (a) dust only and (b) dust with sea salt cases, along with (c) associated nephelometer data.

particles. The sharp minima in the visibility field at 78 hours for the dust only run and at 30 hours for the dust with sea salt run correspond to the presence of a cloudy layer.

It is important to note that during the SHADE campaign, specific values of visibility were not recorded as part of the C-130 instrumentation package. However, the amount of scattered radiation was measured by a nephelometer, and is presented for comparison (figure 4.12, panel c). It is positive to see that the maxima in the nephelometer profile match minima in visibility, with minima corresponding to high visibility regions. So, while it has been shown that the visibility variable is working qualitatively well, quantification of this variable was not possible with the data set used. It is also encouraging that the visible ranges output from the model are reasonable values. It is specifically positive to see that the dusty layer has a visible range of approximately 5km—a value not unexpected in extremely hazy conditions.

4.3 Results from Profile 2 – 24 September 2000

Again, a set of eight model runs was completed in this investigation, with the common threads being the NCEP initialization data, and the vertical dust concentration profile collected on the initial ascent of the C-130 aircraft on the 24th of September 2000 (see figure 4.13). This dust profile differs from the previous profile in the magnitude of the dust concentrations in the dusty layer. Instead of having a profile maximum of 1,889 particles/cm^3, the maximum is only 485 particles/cm^3.

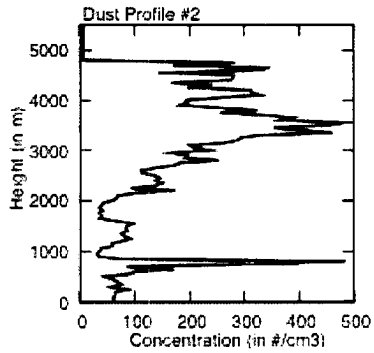

Figure 4.13: Vertical concentration profile for dust profile #2.

4.3.1 Changes in the Temperature Profile

When looking at the temperature and moisture profiles with the new vertical dust concentrations, the same qualitative features are present. Ammonium sulfate has essentially no effect on the temperature and moisture profiles, while sea salt has the ability to allow the temperature inversion to reach greater heights. The differences again lie in the model runs containing mineral dust (figure 4.14). The only feature that is markedly different using a less concentrated dust layer is that the moisture content is now lower than the initialized sounding in and above the dust layer (above about 4,000m), but still displays higher dew points than the model run containing no aerosol effects. It is also expected that with a lower concentration of an absorbing aerosol species, such as mineral dust, the overall temperature changes would be much smaller (see figure 4.16). Instead of heating on the order of 6°C and 10.8°C for 30 and 78 hours respectively, this model run yielded heating of 2.5°C and 3.8°C after 30 and 78 hours of model run time respectively. Again, the maximum heating rates are found where the dust concentrations are elevated (3,500m to 3,700m).

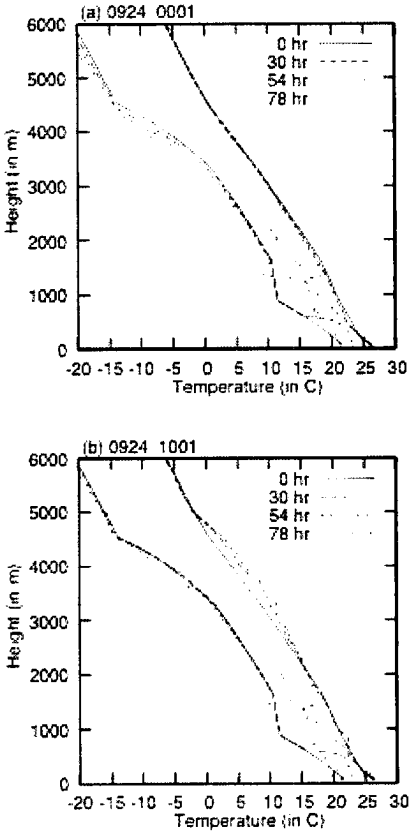

Figure 4.14: Temperature and dew point profiles using profile #2, comparing no dust, and dust cases.

4.3.2 Changes in the Radiation Streams

As with the temperature profiles, the radiation streams have essentially the same qualitative response as they did for the previous dust profile, with the ammonium sulfate and sea salt aerosols having little to no effect. The reduction in outgoing radiation (both short- and longwave) is much lower using dust profile 2, when compared with dust profile 1 (see table 4.2). This newer mineral dust profile presents a reduction of approximately 65% in the overall change to the radiation streams--upward and downward, short- and longwave. Again, the bulk of the change in irradiance happens in the layer below 4,500m, where the bulk of the mineral dust aerosol is present.

	Profile 1	**Profile 2**
Max ΔT, 30hr	6.1°C	2.5°C
Max ΔT, 78hr	10.8°C	3.8°C
ΔLWUP	-24.8W/m^2	-6.2W/m^2
ΔSWUP	-41.3W/m^2	-18.9W/m^2
ΔTOTAL UP	**-66.1W/m^2**	**-25.1W/m^2**
ΔLWDN	+35.2W/m^2	+12.8W/m^2
ΔSWDN	-328.3W/m^2	-108.6W/m^2
ΔTOTAL DN	**-293.1W/m^2**	**-95.8W/m^2**

Table 4.2: Comparison of temperature and radiation stream changes due to dust profiles #1 and #2

4.3.3 Changes in the Maximum Vertical Velocity Profile

It is expected that changes in maximum vertical velocity are much smaller in magnitude here, when compared with dust profile 1, and this does indeed hold true (see figure 4.15). The changes in the maximum vertical velocity show that there is only upward vertical motion in the lower 6,000m of the model domain during the daylight

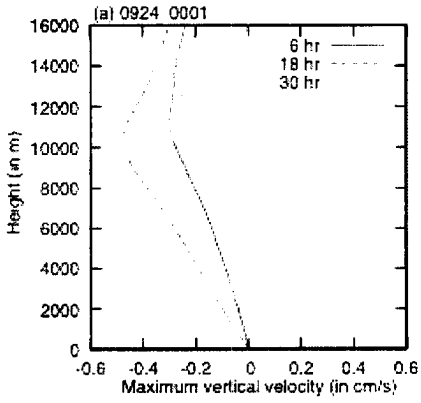

Figure 4.15a: Maximum vertical velocity profile for profile #2 with no aerosols active.

hours. The peak of the upward motion is around 4,000m—the core of the dusty layer. Throughout the remainder of the model domain during the daytime hours, maximum vertical velocity is higher at every grid point, giving more credence to the buoyant heating effect postulation. Again, there were no discernable changes in the maximum vertical velocity field when the radiative impacts of ammonium sulfate or mineral dust were taken into accounted.

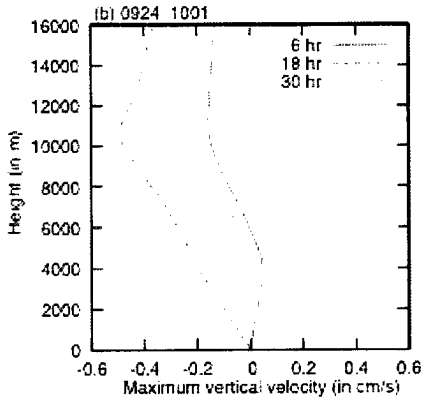

Figure 4.15b: Maximum vertical velocity profile for profile #2 with no mineral dust active.

4.3.4 Investigation into Visibility

The trends in all three fields investigated above are consistent with the results from the visibility. The ammonium sulfate has essentially no impact on modeled visibility, while the sea salt has an impact only in the very lowest few model levels. Only the visibility field from the run containing both sea salt and mineral dust are presented here (figure 4.16). Again, the visibility minima are located where the dust concentrations are the highest (850m, and 3,000 - 4,700m). This time it is also worth noting that the dust layer has not grown in thickness to the extent it did during the profile 1 experiments. This is consistent with

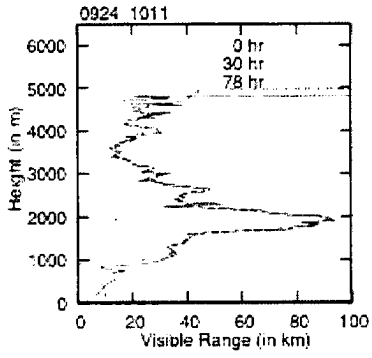

Figure 4.16: Visibility profiles for profile #2 with both sea salt and mineral dust active.

idea that the buoyant heating in the dusty layer was not as strong, and therefore could not allow for the vertical transport of the dust layer as easily as during the profile 1 experiments.

4.4 Results from Profile 3 – 25 September 2000

The dust profile examined here has similar concentration values to that of profile 1, but also has a different structure (figure 4.17). The maximum dust concentration was confined to a layer much lower in the atmosphere than the previous studies—3,878 particles/cm^3 at 1,250m. The location of the dusty layers in the previous runs still contains dust, but the concentration values are between those of profiles 1 and 2. The vertical extent of this dust layer is also slightly higher than in the previous two profiles.

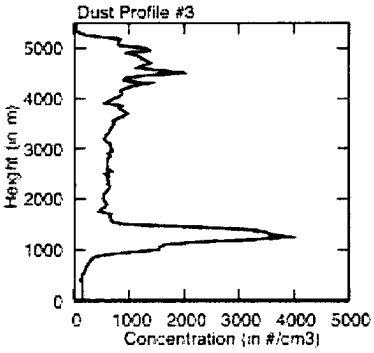

Figure 4.17: Vertical concentration profile for dust profile #3.

4.4.1 Changes in the Temperature Profile

Due to the marked difference in the distribution and location of the dust maxima in profile 3, the associated temperature and moisture profiles exhibited slightly different behavior (Figure 4.18). It has been previously remarked that when mineral dust aerosols are present, the atmosphere heats up due to absorbed solar radiation. This is again the case with dust profile 3. Here, however, the low-level dust maximum allows for the formation of a warmed layer at much lower heights than previously seen. The 3,000m to

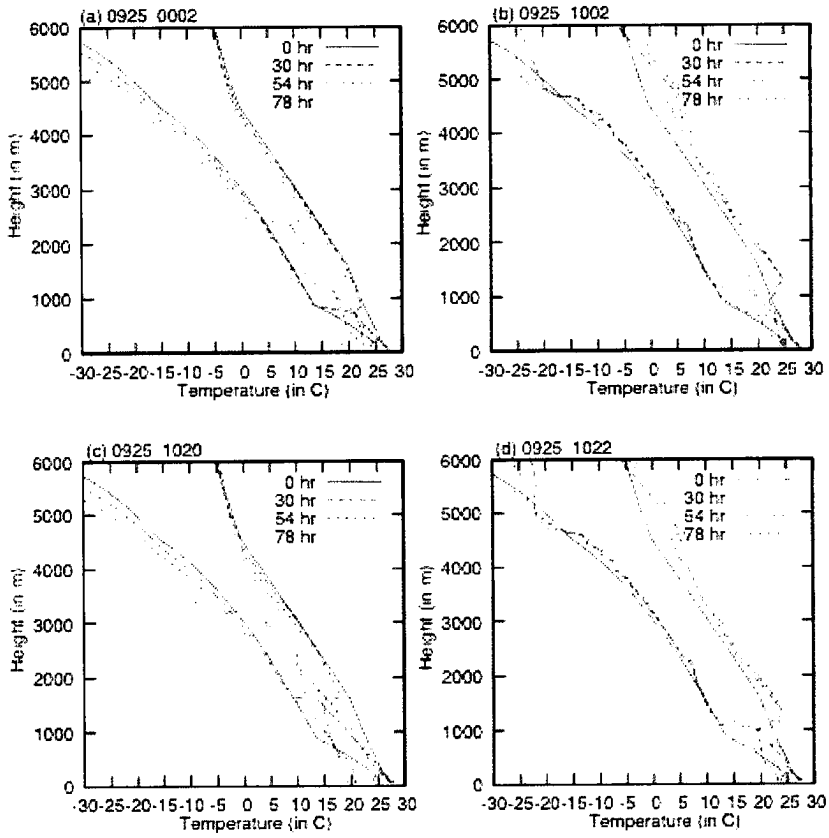

Figure 4.18: Temperature and dew point profiles for selected run using dust profile #3.

5,000m layer still shows copious amounts of atmospheric heating, and moistening when the dust is radiatively active. Also, as seen previously, the radiative modifications due to the presence of sea salt causes the unrealistic inversion height to increase. The main difference in this set of model runs versus the previous sets is that the low-level dust layer is actually forming a strong enough temperature inversion to inhibit the unrealistic growth of the boundary layer. This is true whether or not the sea salt is radiatively active. Unfortunately, heating rate comparisons in the highly concentrated dust layer cannot be made during these sets of model runs. This is because the height of the temperature inversion in the corresponding non-dust cases is above the level of the maximum dust

concentration. The broader dust layer from 3,000m to 5,000m shows a change in heating of nearly 9°C after the full 78-hour model run time.

4.4.2 Changes to the Radiation Streams

Since the vertical dust profile is markedly different than the previous two, it is illustrative to view the radiation streams for the no aerosol case juxtaposed against the case with active mineral dust (figure 4.19). The major change is visible in the downwelling shortwave radiation stream. Beginning at 5,200m, the reduction in downwelling shortwave radiation is greatly increased due to the presence of the Saharan dust layer. There is also a sharp kink in the curve at 1,500m due to the highly concentrated dust layer at 1,250m. The downwelling longwave radiation curve is quite similar, except in the lower 5,000m, again due to the presence of the mineral dust. The magnitudes of the overall changes when compared with profile 1 are shown in table 4.3. As expected, the effects of profile 3 are

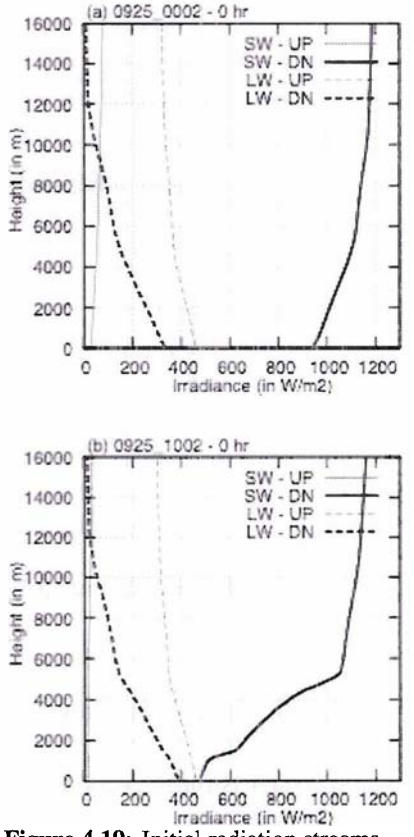

Figure 4.19: Initial radiation streams for profile 3 cases (a) without dust and (b) with dust.

	Profile 1	Profile 3
ΔLWUP	-24.8W/m^2	-28.5W/m^2
ΔSWUP	-41.3W/m^2	-47.4W/m^2
ΔTOTAL UP	**-66.1W/m^2**	**-75.9W/m^2**
ΔLWDN	+35.2W/m^2	+55.0W/m^2
ΔSWDN	-328.3W/m^2	-470.0W/m^2
ΔTOTAL DN	**-293.1W/m^2**	**-415.0W/m^2**

Table 4.3: Comparison of radiation stream changes due to dust profiles #1 and #3

greater in magnitude than for profile 1, but the value of the direct radiative effect ($470W/m^2$) is even farther from the maximum values measured during the SHADE by Haywood, et. al (2003) of $129W/m^2$.

4.4.3 Changes in the Maximum Vertical Velocity Profile

The changes in the maximum vertical velocity profile for profile 3 (not shown) are nearly identical to profile 1. While the no aerosol case has a completely subsiding profile over the 30 hours investigated, the maximum vertical velocity indicates upward motion for the two daytime profiles. Again, it is the author's opinion that this upward motion is due to heating within the absorbing dust layer, causing very small amounts of vertical buoyant motion. It should be pointed out that the maximum vertical velocities are still on the order of millimeters per second.

4.4.4 Investigation into Visibility

Again, the changes in visibility that are present are a result of either mineral dust or sea salt. The visibility impact of sea salt is essentially only in the lower 1,000m of the atmosphere. Figure 4.23 shows the visibility impact of activating both sea salt and mineral dust. The visibility minimum for this case reached down to 1.4km in the heart of the low-level dust layer, with values varying between 5 and 9km in the more elevated layer. As for the nephelometer, the data show that scattering was decreasing with increasing altitude above the dust maximum at 1250m. Unfortunately, the visibility also shows a decrease with increasing altitude (the opposite should in general be true). This should not be a huge cause for alarm, as the issue could very well lie in the fact that we

are assuming a constant size profile throughout the entire depth of the model domain (log-normal profile with specified median radii). It would follow that larger particles would not necessarily be able to attain the height that smaller particles do, or that long term, larger particles would be more prone to gravitational settling than their smaller counterparts. This would mean that overprediction of visibility would be possible if this effect were to occur to a large extent before the model was initialized, as the model initially assumes that the same size profiles are present at all altitudes.

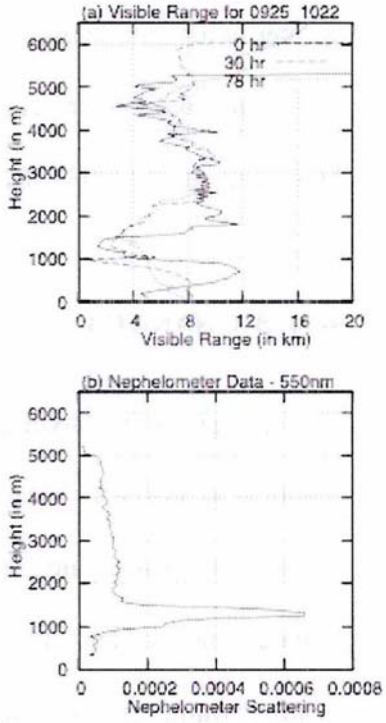

Figure 4.20: Visible range for profile #3 case containing both sea salt and mineral dust, with associated nephelometer profile.

4.5 Discussion of Results

Overall, it would appear that a few general conclusions can be made about the radiation module itself. It appears as though the amount of calculation time that the model expends on determining the radiative effect of ammonium sulfate is not worth it. This is especially true if the desire is to get this module operational for real-time forecasting. The second issue pertains to the radiation calculations due to sea salt. While there was very little to mention as far as the changes to most of the radiation streams, near the surface, the downwelling longwave streams show large changes. This is most likely due to the fact that the amount of scattered and absorbed radiation has to do with areal cross-sections; specifically that sea salt particles can rapidly deliquesce to increase the areal

cross-section with a strong infrared absorber—water. As for mineral dust, the remaining four sections discuss the findings that could be of major consequence.

4.5.1 Mineral Dust Effects on Temperature and Moisture profiles

As far as understanding the changes to the temperature and moisture profiles that were caused by the mineral dust, most are understood with relative certainly. It is postulated that when dust was present in large quantities, the moisture content as measured by the dew point always increased over the non-dust model runs, due to the large-scale vertical ascent. This ascent could be responsible for bringing higher moisture content air into the dusty layers, where maximum vertical velocities are greatest.

As for the changes in the temperature profiles during the model runs containing the aerosol radiative effect of mineral dust, the results make sense. The largest temperature changes were due to absorption of solar energy by the mineral dust during the daytime hours. Very little change in direction was noted with the shortwave energy streams, as no large increase of upward bound solar radiation was seen in the irradiance profiles. That combined with the fact that the asymmetry factors as computed by the Mie code were all close to unity (positive), indicates that any scattering caused by the mineral dust would be in the forward direction. The temperature changes ranged from approximately 1-3°C/day, most of which was a direct result of radiation absorption in the shortwave. It would be useful to look at the changes in the temperature profiles of a dust-laden layer in a three-dimensional simulation where large scale forcing and the u, v and w components of the wind were all predicted. The continued temperature increase that was seen in these

model runs would then most likely find an equilibrium with the environment in which they are found.

The other useful feature found in the temperature profile changes was the formation of a strong inversion due to highly concentrated dust in profile 3. If this low-level inversion were strong enough, it could very well suppress all vertical motion through the layer, and hence show a systematic shutdown of all convection (shallow or deep). If this inversion were not strong enough to cap convection, then the main dust layers in the 3,000m to 5,000m ranges would certainly be able to suppress deep convection. If an elevated heated layer were formed with the presence of mineral dust, this would reduce the amount of convective available potential energy (CAPE), which could in turn suppress vigorous convection. If this change in CAPE were large enough, it could also have the possibility of reducing the amount of precipitation that could be derived from these storms. This explanation of reduced surface precipitation is consistent with a previous RAMS study outlining dust effects on deep convection from a standpoint of changing the microphysics of the convective cells (van den Heever, et. al 2005).

4.5.2 Changes in the Radiation Streams

All of the conclusions that can be drawn from the work pertaining to the radiative impact of mineral dust can be boiled down to one word...absorption. Mineral dust had the distinction of reducing the intensity of all upward bound radiation streams. In fact mineral dust reduced outgoing longwave radiation by 25W/m^2, 6W/m^2 and 29W/m^2 for profiles 1, 2 and 3 respectively. However, the reduction in outgoing longwave radiation

was determined to be approximately 6.5W/m^2 for this given dust outbreak (Highwood, et. al, 2003). The same trend was seen in the downwelling solar radiation stream as well. The maximum values that of shortwave reduction due to dust during the SHADE campaign were on the order of –130W/m^2 (Haywood, et. al, 2003), with modeled values from this study using the different mineral dust profiles being –328W/m^2, -109W/m^2 and –470W/m^2 respectively. Since the values all of these modeled values were well above those estimated by previous works, it should follow that a sensitivity study should be performed allowing for changes in the imaginary part of the refractive index (see Chapter 5). Regardless of the magnitude of the results, it is clear that mineral dust will reduce surface solar radiation, while trapping radiation in the atmosphere, and acting as a greenhouse aerosol.

4.5.3 Changes in the Maximum Vertical Velocity Profile

Mineral dust did have the ability to change the overall maximum vertical velocity profile, from the state where no aerosols were considered. Because the maximum vertical velocity was increased over the control runs during daylight hours, it is assumed that this is due to small scale buoyant heating. It can also be seen that the dusty layer was transported vertically with time, a possible physical manifestation of the buoyant heating effect. The same effect was not visible during the nighttime hours, further corroborating the buoyant heating hypothesis. This hypothesis does not necessarily contradict the hypothesis of Miller, et. al. (2004) that increased aerosols would decrease turbulent boundary layer motions. In fact the depth of the boundary layer (while quite unrealistic)

was shallower in cases containing high concentrations of mineral dust, leading credence to Miller, et. al's hypothesis as well.

4.5.4 Investigation into Visibility

The new visible range variable calculated by RAMS, seems to be working. Unfortunately, the only verifiable result pertaining to visibility came from a nephelometer. These results show that the visible range variable is acting in the correct sense, while the magnitudes were not able to be rigorously tested. The values of visible range within the dusty layers do seem to be "reasonable", expecting that a hazy layer would have visibilities in the neighborhood of 5km.

CHAPTER 5 –SENSITIVITY STUDIES

5.1 MODEL SENSITIVITY TO INITIAL SEA SALT CONCENTRATIONS

After seeing that the radiative effect of sea salt was so high for such low concentrations, and after seeing that the model was reproducing anomalously deep marine boundary layers, an investigation was launched to determine what effect the initial sea salt concentrations had on overall model results. The sensitivity study was done such that all eight model runs of profile 1 were re-run twice, each with only one change—a reduction in the initial GCCN concentration profile. The first set of model runs in this sensitivity study had a reduction in GCCN by a factor of 5—the second set was reduced by another factor of 5, so that the surface values of GCCN were 1.0/cm^3 and 0.2/cm^3 respectively (see figure 5.1), compared to the initial value of 5/cm^3. The following sub-sections describe the changes from the "baseline" set of model runs.

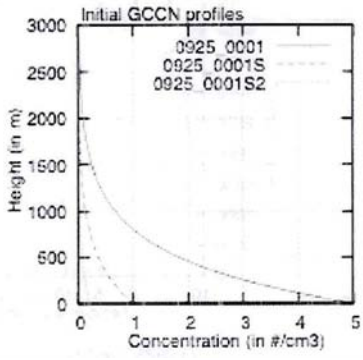

Figure 5.1: Initial GCCN profile used in the sensitivity study.

5.1.1 CHANGES IN THE TEMPERATURE AND MOISTURE PROFILES

Before even investigating the radiative effect of aerosols on the temperature and moisture profiles, it is important to see what changes take place by only changing the GCCN

profile within the model. Figure 5.2 shows that as the amount of GCCN in the model decreases, so does the anomalously high mixed layer, until the mixed layer is a much more reasonable 500m after 78 hours of simulated time. Based on this result alone, it is obvious that a reasonable estimate of GCCN needs to be made before the simulations begin. The resulting anomalously thick boundary layers would not have materialized in these model runs if lower initial GCCN concentrations were used.

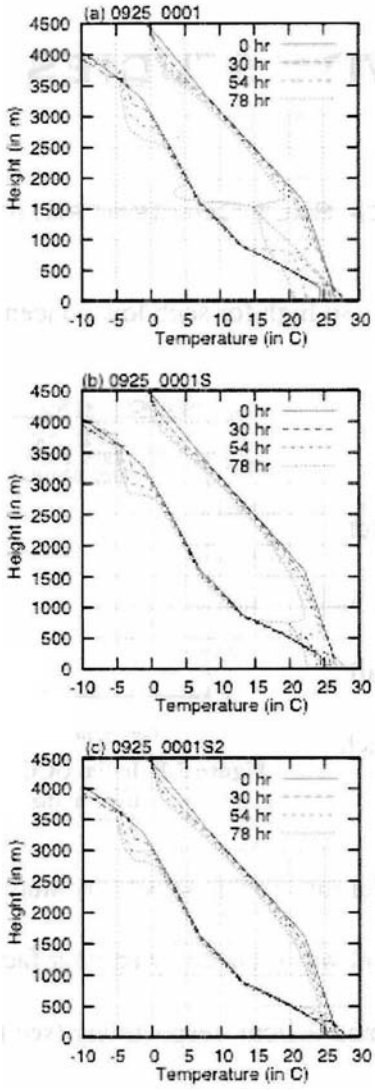

Figure 5.2: Temperature and dew point profiles for the three no aerosol cases for the sea salt sensitivity study.

Another interesting feature is present once the GCCN concentrations are reduced. In the case where the surface GCCN concentration is initially 0.2/cm^3, two of the three aerosol species actually cause the boundary layer to be slightly thicker, with ammonium sulfate having no appreciable effect (it should be noted that the boundary layer thickness was determined by finding the level at which the layer temperature increased by at least 0.2°C from the previous layer). For example, the boundary layer thickness at 78 hours for the no aerosol case (0925_0001S2) was 500m. If the radiative effect of sea salt was added to the blank case (0925_1010S2), the boundary layer thickness became 850m. If the mineral dust effect was also added (0925_1011S2), the boundary layer thickness became 1,000m.

5.1.2 Changes in the Radiation Streams

As mentioned in Chapter 4, there was not a lot of radiative effect felt by the presence of sea salt in the model. The only radiation stream that showed any appreciable change due to the presence of sea salt was the downwelling longwave stream. When the concentration of sea salt was reduced, so was the strength of the longwave surface forcing; the forcing was reduced from 24.8W/m^2 to 5.4W/m^2 with the first 5-fold reduction in concentration, and again to 1.1W/m^2 with the second 5-fold reduction (see figure 5.3). It is not surprising to see that the downward radiative forcings of sea salt look nearly identical to the concentration profiles provided in figure 5.1.

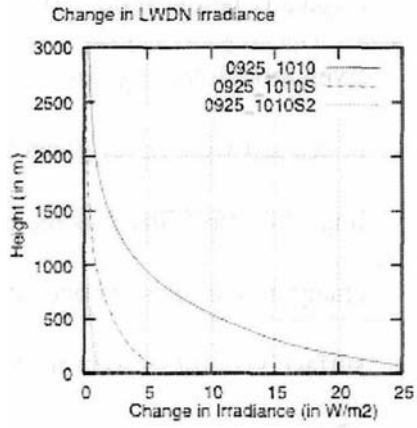

Figure 5.3: Changes in the dowwelling longwave streams to due changes in sea salt concentrations.

5.1.3 Changes in the Maximum Vertical Velocity Profiles

After reviewing the data, there are no qualitative differences in the maximum vertical velocity fields when the initial concentration of GCCN (sea salt) is varied. The buoyant effect due to heating caused by the presence of mineral dust still exists and is of the same magnitude.

5.1.4 Investigation into Visibility

Changes in the GCCN profiles and hence the profiles in sea salt, cause major changes in the visibility in the lower level of the model domain (typically below about 2,000m, see figure 5.4). Even though the highest surface concentrations of sea salt were never greater than 5/cm^3, their impact on visibility was incredibly large. By changing the sea salt concentrations, the initial surface visibilities were increased from 4.4km to 17.5km to 43.7km, with each successive decrease. It is evident that if sea salt were to be included in the visibility calculations, good initialization values for the vertical profile of sea salt would be required to get reasonable and believable visibility values.

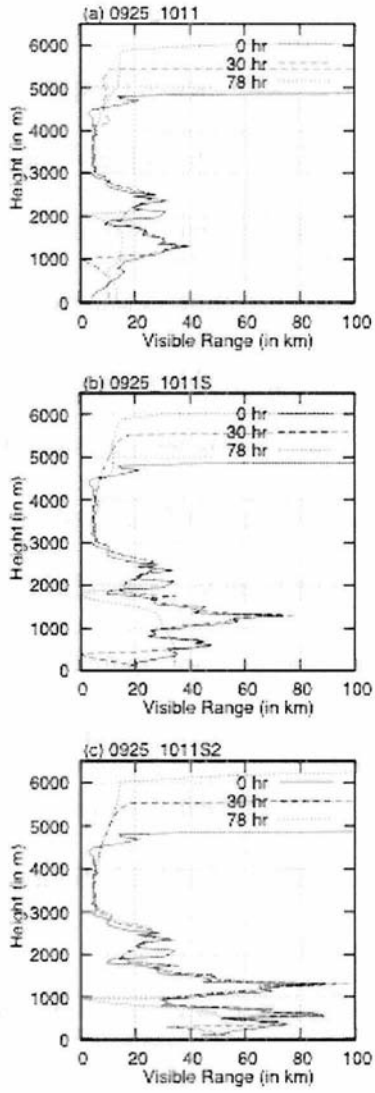

Figure 5.4: Visible ranges for three sea salt cases with mineral dust.

5.2 Model Sensitivity to Changes in Refractive Index

As seen in Chapter 4, the values that were obtained from the model for the reduction in surface bound solar radiation were 3-4 times greater than the values determined through instrumentation over the same period. The data collected from the particle soot absorption photometer (PSAP), along with the radiative forcings that were collected

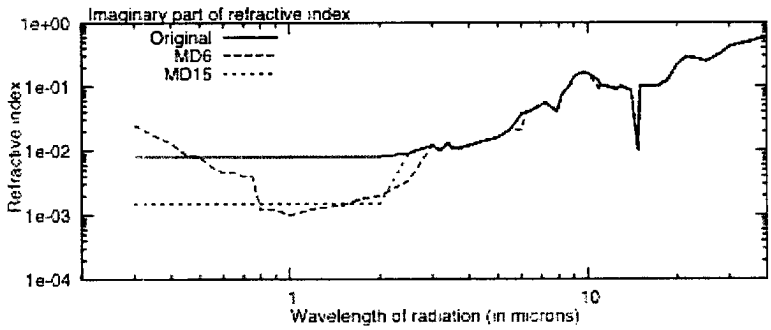

Figure 5.5: Imaginary part of the refractive index used in the dust sensitivity study.

during SHADE, allowed Haywood, et. al (2003) to make this change to the refractive index. The modifications were then made to the imaginary part of the refractive index of mineral dust in the 0.3μm – 2.0μm range from 0.008*i* to 0.0015*i*. Based on this, there are two new sets of refractive indices that were used for the mineral dust sensitivity study (Figure 5.5). The first new profile, MD6 (so-called due to variable number in the Mie subroutine) was called "mineral," whereas the original material was referred to as "dust-like." The MD6 profile differs quite markedly from the original, in the wavelength range smaller than 3μm. The rest of the imaginary refractive index profile was quite similar. The MD15 (so-called because of the specific change in the refractive index from 0.008*i* to 0.0015*i*) is purposefully identical to the original profile at wavelengths greater than 2μm, but reduced at smaller wavelengths. The changes caused by these refractive index profiles are displayed in the following sections.

5.2.1 Changes in the Temperature and Moisture Profiles

The new refractive index profiles appear to affect only the magnitude of the change to the temperature and moisture profiles. To start, the moistening of the layers above the main

dust layer (4,000m to 6,000m) was reduced in both cases over the original runs, although moistening was still present. However, the major difference in this sensitivity test to temperatures, came in the form of reduced temperature changes in and near the main dust layer (3,000m to 5,000m) (see figure 5.6). The maximum temperature change after 30 hours of simulation time fell from +6.1°C to +4.4°C for the MD6 case and +3.6°C for the MD15 case (see figure 5.7). Similar relative changes were seen at 78 hours as well, with the changes falling from +10.8°C, to +7.8°C in the MD6 case and to +6.0°C for the MD15 case. The temperature changes in the other layers, while of much smaller magnitude to begin with, still showed similar relative decreases.

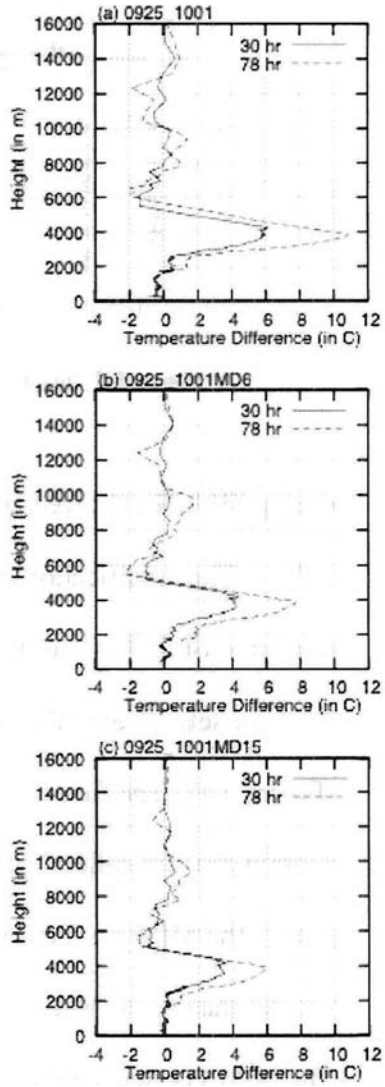

Figure 5.6: Temperature changes for mineral dust using different refractive index profiles.

5.2.2 Changes in the Radiation Streams

It should first be noted that there are absolutely no changes in the initial longwave radiation streams, because the only changes to the refractive indices were in the shortwave (i.e., less than 4.54μm). There were changes, however, in the downwelling longwave profiles due to slightly lower temperatures in the dust-laden layers. The initial profile did not change, but the subsequent profiles showed changes as large as 14W/m^2 in

reduced downwelling forcing in at its peak. The remainder of the analysis was again limited to the initial time period, as no clouds were yet present, and the forcings caused by the radiative activity of the mineral dust profiles had not been fed back into the model. Only minor changes were seen in the upward bound forcings at the model top, with the largest change being in the shortwave (due to changes in refractive index). When looking at the downwelling radiation streams however, the major change is noted in table 5.1 in bold. The shortwave forcing due to the presence of mineral dust was reduced from $-328.3 W/m^2$ in the original case to $-240.1 W/m^2$ in the MD6 case ("mineral"). When the specific changes recommended by Haywood, et. al (2003) were implemented the radiative forcing dropped all the way to only $-99.1 W/m^2$. This forcing is now within the maximum recorded forcing of $-129 W/m^2$.

	Profile 1	MD6	MD15
Max ΔT, 30hr	+6.1°C	+4.4°C	+3.6°C
Max ΔT, 78hr	+10.8°C	+7.8°C	+6.0°C
ΔLWUP	$-24.8 W/m^2$	$-24.3 W/m^2$	$-24.8 W/m^2$
ΔSWUP	$-41.3 W/m^2$	$-36.5 W/m^2$	$-26.2 W/m^2$
ΔTOTAL UP	$-66.1 W/m^2$	$-60.8 W/m^2$	$-51.0 W/m^2$
ΔLWDN	$+35.2 W/m^2$	$+34.4 W/m^2$	$+35.2 W/m^2$
ΔSWDN	**$-328.3 W/m^2$**	**$-240.1 W/m^2$**	**$-99.1 W/m^2$**
ΔTOTAL DN	$-293.1 W/m^2$	$-205.7 W/m^2$	$-63.9 W/m^2$

Table 5.1: Comparison of temperature and radiation stream changes due to changes in the refractive index of mineral dust

5.2.3 Changes in the Maximum Vertical Velocity Profiles

There were only slight changes in the maximum vertical velocity profiles when the dust refractive index was switched to that of MD6 (Figure 5.8). The maximum vertical velocities were slightly smaller, but still showed similar trends of being higher during he daytime heating hours and lower during the nighttime cooling. When the MD15 profile was used, there were only slight variations from the no-aerosol run—the daytime values

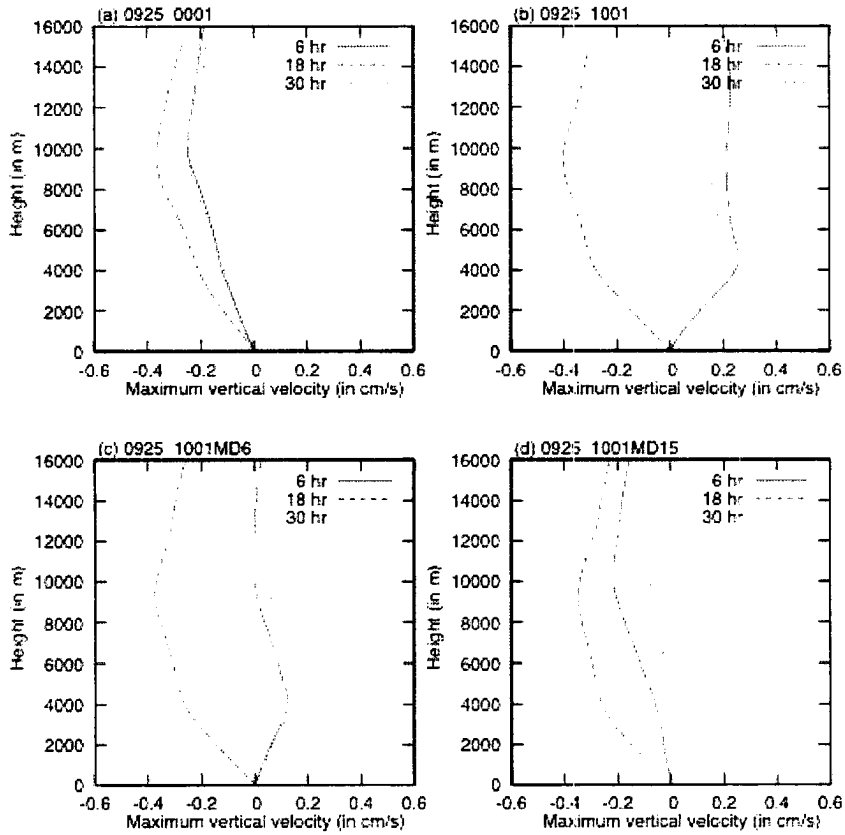

Figure 5.7: Maximum vertical velocity profiles showing differences due to refractive index of dust.

still showed an increase with the mineral dust aerosols present, while the nighttime values also showed an increase. Again, if these changes are assumed to be due to a localized buoyant heating effect, this is consistent with the previous theory, as the new refractive index profiles for dust allowed for reduced atmospheric heating.

5.2.4 Investigation into Visibility

After looking at the new visibility fields for each of the two new refractive index profiles for mineral dust, only minor changes were perceptible. These changes were not due to changes in the refractive index, but due to changes in the radiative feedbacks into the

microphysics package. Essentially the changes in visibility were caused by development of different wind and advection patterns from the initial case.

5.3 Discussion of Results

The two sensitivity studies showed that the model is certainly sensitive to initial concentrations of sea salt, as well as the imaginary part of the refractive index of mineral dust. The main issue surrounding further use of sea salt as a radiatively active species is that specific vertical profiles of sea salt need to be known. If the initial concentrations were reduced, the formation of the anomalously thick boundary layer was not seen. Of course, this boundary layer thickness issue could also be solved by 3-dimensional testing with large scale atmospheric forcing. Regardless of the cause of the anomalously thick boundary layer, once the concentrations of sea salt particles are well known then the variable should be re-tested for inclusion in upcoming model runs. Another problem in this initial attempt at using radiatively active sea salt, is that it was tied directly to the microphysics, by having GCCN as a proxy for sea salt concentrations. As current avenues of research come to fruition, separate source and sink functions for sea salt concentrations will become available—and they will be fully prognostic in future versions of RAMS. But until that point, it is the author's suggestion that sea salt NOT be a radiatively active species, due to extremely large uncertainties in concentrations, and the microphysical feedbacks seen in this sensitivity study.

The investigation into changing the imaginary (absorptive) part of the refractive index yielded much more successful results. The initial refractive index profile gave a downwelling shortwave radiative forcing that was 3-4 times greater than recorded with

shortwave broadband radiometers (Haywood, et. al, 2003). The value for profile 1 of $-328.3 W/m^2$ was reduced to $-99.1 W/m^2$ when the imaginary part of the mineral dust refractive index was reduced from $0.008i$ to $0.0015i$ for all radiation smaller than 2μm in wavelength. This reduction in the direct radiative effect of mineral dust by 70% can also be extrapolated to the "heavier" dust profile. If that profile were affected in a similar manner to mineral dust profile 1, the downwelling shortwave forcing would be reduced from $-470 W/m^2$ to $-141 W/m^2$. This new forcing of $-141 W/m^2$ for the heaviest profile tested would now compare extremely favorably to the $-129 \pm 5 W/m^2$ recorded as the maximum direct radiative effect. Based on this testing alone, the newest dust tests using the refractive index of MD15 would be recommended for future use of the mineral dust aerosol radiative effect.

CHAPTER 6 –CONCLUSIONS

6.1 SUMMARY AND CONCLUSIONS

A new module was created for the Regional Atmospheric Modeling System (RAMS) that now allows for the prediction of the radiative effect of aerosols. This research fills needs in both the military realm, for the prediction of visibility degradation caused by mineral dust aerosols, and in the civilian realm, by allowing for a more complete numerical weather prediction system.

6.1.1 SUMMARY OF WORK

RAMS was modified by creating a new module that can be accessed when the user desires to include the radiative effects of three atmospheric aerosol species: ammonium sulfate, sea salt and mineral dust. Each of these species is represented by a lognormal size distribution, with known overall concentration and median radius. The new module then determines the amount and direction of radiation scattering as well as the amount of radiation absorption by the aerosol species using an off-line Mie theory subroutine. This effect is then combined with the other radiative effects already included in RAMS (those by hydrometeors, cloud droplets, and absorptive gases such as water vapor, carbon dioxide and ozone), to yield an updated total radiative effect. This is then fed back into the model to immediately update the temperature streams, which allow for the presence

of these aerosol species to be accounted for in the numerical weather prediction framework.

The model was run in an LES-type mode with two spatial dimensions, a vertical dimension, with 50m resolution in the aerosol laden layers, and an east-west horizontal dimension with 100m resolution. The model was run for 78 hours with a time step of 2 seconds. NCEP reanalysis data was used to initialize the model in a horizontally homogeneous fashion. The model was tested using assumed profiles for the atmospheric concentrations of both ammonium sulfate and sea salt. The Saharan Dust Experiment (SHADE) data was used to determine vertical profiles of mineral dust concentrations. Three different dust loadings were the basis for the initial model testing, a moderate case (profile 1), a light case (profile 2) and a heavy case (profile 3). For each mineral dust profile, a set of eight model runs was completed, using a binary on-off switch for each of the three aerosol species.

Sensitivity tests were also completed. During the initial three sets of model runs, the problem of anomalously thick marine boundary layers was seen. To check for a remedy to this issue, GCCN concentrations were modified to check for any differences in the development of this inversion (and any other effects this caused), as GCCN was used as a proxy for sea salt concentrations. This testing showed a reduction in the anomalously high boundary layer height with reduction of the sea salt concentrations. A second set of sensitivity tests were completed, by changing the imaginary part of the refractive index of mineral dust. By changing the refractive index in the shortwave to recommended values,

the reduction in downwelling solar radiation was brought quite close to recorded values from the SHADE campaign (Haywood, et. al, 2003).

6.1.2 Conclusions

After having completed all the initial model runs, as well as the sensitivity testing, a few conclusions can be gleaned from the previous chapters. First, the temperature and radiation stream modification due to the presence of atmospheric aerosols is working in the correct sense, although the magnitudes of the effects are still up for debate. In all layers where mineral dust was present, the radiation streams (both long- and shortwave) were reduced in intensity, due to the strongly absorbing nature of mineral dust. The downwelling shortwave reduction by the dusty layers seemed to be within reasonable distance of the values computed by Haywood, et. al (2003) during the SHADE campaign, especially once the refractive index of mineral dust was properly adjusted. The upwelling longwave reduction by mineral dust was quite a bit greater than seen during SHADE (Highwood, et. al, 2003); this problem was never fully resolved. In general, the dust particles did not cause much backscatter of radiation, as the particle radii were overall much smaller than the wavelengths of the radiation in question, allowing for general forward scattering (diffusion) of the radiation. Sea salt caused only minor changes in the longwave streams near the surface, which was most likely due to the large mass of the particles, as well as the adsorbed water. Ammonium sulfate showed essentially no effect to the temperature or radiation streams.

After having introduced the changes to the radiation streams as a result of the aerosols, a visual range variable using the Koschmeider equation was employed. Collected

nephelometer data during SHADE, illustrated that the visibility variable was also acting in the correct sense (lower visibility with higher aerosol loadings), but again the actual values recovered from the model are not certain. While the visibility predicted in the dusty layers seemed reasonable, there is nothing in the SHADE data set that would allow for direct comparison of visibility values in the dusty layer.

As far as the model itself goes, the overall conclusion can be given that the radiation subroutines are now producing changes to RAMS that appear to be reasonable and accurate. There will certainly need to be some work done on tuning the various parameters within the radiation subroutines in order to get results that are quantitatively correct (see section 6.2). As current avenues of research using RAMS are completed, ammonium sulfate and sea salt will have their own source and sink functions within the model and will not be inextricably tied to the microphysics subroutines through the concentration values of CCN and GCCN. This will then eliminate the uncertainty of knowing the surface concentrations of the active radiatively active aerosol species. Despite this eventual change, one suggestion for future use of the radiation model is simple, the inclusion of ammonium sulfate as a radiatively active species should be carefully evaluated, as the run-time costs may exceed the usefulness of calculating its radiative contribution, especially if the model is to be run in real-time. The inclusion of sea salt as radiatively active should also be carefully evaluated, as uncertain profiles of sea salt could lead to large changes in the downwelling longwave radiation field.

6.1.3 Scientific Implications of the Work

Despite the fact that this was a first pass at adding the aerosol radiative effect to RAMS, there are also some general scientific conclusions that can be drawn from this modeling study. First of all, with an overall reduction in the amount of radiation leaving the model top, it can be assumed that mineral dust is therefore acting as a greenhouse aerosol; energy is being trapped in the dusty layers, and is not able to escape the atmosphere. The results of this paper would therefore indicate that the radiative forcing of mineral dust aerosols is positive, where as the International Panel of Climate Change sees mineral dust forcing as uncertain in overall direction (*IPCC, 2001*). Also, this trapped radiation represents radiation that would otherwise have reached the surface. This reduction in surface radiation could mean slight reduction in surface temperatures. These arguments then lead to the second point of this particular argument--that higher mid-level temperatures, combined with lower surface temperatures would work to generally reduce upward motion within the atmosphere (by decreasing ambient lapse rates), which could be quantified by a reduction in convective available potential energy (CAPE). This CAPE reduction could then be manifested in reduction of surface precipitation, further augmenting the results of van den Heever, et. al (2005). This hypothesis has not been tested, and is merely an assertion based on the changes in the atmospheric temperature profiles presented in this study.

6.2 Recommendations for Future Work

The new radiation module is certainly working qualitatively well, but in order to be used as a quantitative model, a few suggestions on future direction of it are necessary. First, in order to believe the actual values of the changes in the temperature field with time, it would be necessary to have some large scale forcing present. All of the presented model runs were completed with no outside forcing; the NCEP initial conditions were given, and the model was allowed to develop on its own for the entire 78-hour model runs. Three-dimensional testing with nested grids containing aerosol information would be useful, as it would allow for more quantitative prediction on the heating effect within the dusty layers. This 3-D testing could also highlight the model's ability to see small-scale dust features, and to show the value of the prognostic visibility variable, once visible range data has been collected.

Secondly, the values of refractive index are extremely important to the overall treatment of the aerosol radiative effect. The problem of poor data was highlighted by both Haywood, et. al (2003 and Highwood, et. al (2003), wherein they explained that refractive index values remain the largest hurdle to accurate representation of aerosols within numerical weather prediction frameworks. In this particular study the change in the imaginary part of the refractive in the shortwave dramatically changed the amount of downwelling solar radiation, which was absorbed in the dust-laden layers. The problem of overprediction on the longwave radiative effect is most likely rooted in highly uncertain values of the imaginary part of the refractive index of mineral dust in the longwave (Highwood, et. al, 2003). In order to have more accurate results from this

module, more accurate refractive index values need to be obtained for any species that is desired to be in the radiation module. Since it is well known that mineral dust has a highly variable refractive index based on source region, this too should be understood, and taken into account when the radiation module is to be run.

Once the above recommendations have been implemented, further testing should be done to see if the new model can corroborate the precipitation suppression results from van den Heever, et. al (2005). The results from that paper were obtained by varying concentrations of CCN, GCCN and IFN in the model, where changes in IFN concentrations followed changes in the mineral dust concentrations. The result achieved was an overall reduction in surface precipitation when the IFN concentrations were elevated—a result achieved using changes in the microphysics only. By also allowing changes in the radiation, the above hypothesis about reduction in CAPE (section 6.1.3) could be tested. The results from the new version of RAMS would become more complete, and should therefore be tested against the changes in IFN concentrations from van den Heever, et. al (2005) to see how the model outputs compare, and if the precipitation suppression is present in the two sets of model runs.

REFERENCES

Andrews, E., P.J. Sheridan, J.A. Ogren and R. Ferrare, *In situ* Aerosol Profiles over the Southern Great Plains cloud and radiation test bed site: 1. Aerosol optical properties, *J. Geophys. Res.*, Vol. 109, No. D06, 24 March 2004.

Arakawa, A. and V.R. Lamb, A Potential Enstrophy and Energy Conserving Scheme for the Shallow Water Equations, *Mon. Wea. Rev.*, Vol. 109, pp. 18-36, 1981.

Boucher, O. and T.L. Anderson, General circulation model assessment of the sensitivity of direct climate forcing by anthropogenic sulfate aerosols to aerosol size and chemistry, *J. Geophys. Res.*, Vol. 100, No. D12, pp. 26,117-26,134, 20 December 1995.

Chin, M. and Jacob, D.J., Anthropogenic and natural contributions to tropospheric sulfate: A global model analysis, *J. Geophys. Res.*, Vol. 101, No. D13, pp. 18,691-18,699, 20 August 1996.

Chin, M., R.B. Rood, S.J. Lin, J.F. Mueller and A.M. Thompson, Atmospheric sulfur cycle simulated in the global model GOCART: Model description and global properties, *J. Geophys. Res.*, Vol. 105, No. D20, pp. 24,671-24,687, 27 October 2000.

Chin, M. P. Ginoux, S. Kinne, O. Torres, B.N. Holben, B.N. Duncan, R.V. Martin, J.A. Logan, A. Higurashi, T. Nakajima, Tropospheric Aerosol Optical Thickness from the GOCART Model and Comparisons with Satellite and Sun Photometer Measurements, *J. Atmos. Sci.*, Vol. 59, pp. 461-483, 2002.

Clark, T.L., A small-scale dynamic model using a terrain-following coordinate transformation, *J. Comput. Phys.*, Vol. 24, pp. 186-215, 1977.

Conant, W.C., A. Nenes, and J.H. Seinfeld, Black Carbon radiative heating effects on cloud microphysics and implications for the aerosol indirect effect 1. Extended Koehler theory, *J. Geophys. Res.*, Vol. 107, No. D21, 2002.

Cotton, W.R., R.A. Pielke Sr., R.L. Walko, G.E. Liston, C.J. Trembeck, H. Jiang, R.L. McAnelly, J.Y. Harrington, M.E. Nicholls, G.G. Carrio and J.O. McFadden, RAMS 2001: Current status and future directions, *Meteorol. Atmos. Phys.*, Vol. 82, pp. 5-29, 2003.

d'Almeida, G.A., P. Koepke, E.P. Shettle, *Atmospheric aerosols: global climatology and radiative characteristics*, A. Deepak Publishing, Hampton, VA, 580pp., 1991.

Deardorff, J.W., Stratocumulus-capped mixed layers derived from a three-dimensional model, *Boundary Later Meteorology*, Vol. 18, pp. 495-527, 1980.

Erickson III, D.J., J.J. Walton, S.J. Ghan, and J.E. Penner, Three-dimensional modeling of the global atmospheric sulfur cycle: A first step, *Atmos. Env.*, Vol. 25A, No. 11, pp. 2,513-2,520, 1991.

Gal-Chen, T. and R.C.J. Somerville, On the use of a coordinate transformation for the solution of the Navier Stokes equations, *J. Comput. Phys.*, Vol. 17, pp. 209-228, 1975.

Ginoux, P., M. Chin, I. Tegen, J.M. Prospero, B. Holben, O. Dubovik, S-J. Lin, Sources and distributions of dust aerosols simulated with the GOCART model, *J. Geophys. Res.*, Vol. 106, No. D17, pp. 20,255-20,273, 16 September 2001.

Harrington, J.Y., The effects of radiative and microphysical processes on simulated warm and transition season arctic stratus clouds, PhD Dissertation, Atmos. Sci. paper no. 637, Colorado State University, Fort Collins, CO, 1997.

Haywood, J., P. Francis, S. Osborne, M. Glew, N. Loeb, E. Highwood, D. Tanre, G. Myhre, P. Formenti and E. Hirst, Radiative properties and direct radiative effect of Saharan dust measured by the C-130 aircraft during SHADE: 1. Solar Spectrum, *J. Geophys. Res.*, Vol. 108, No. D18, 18 July 2003.

Highwood, E.J., J.M. Haywood, M.D. Silverstone, S.M. Newman, J.P. Taylor, Radiative properties and direct effect of Saharan dist measured by the C-130 aircraft during the Saharan Dust Experiment (SHADE): 2. Terrestrial Spectrum, *J. Geophys. Res.*, Vol. 108, No. D18, 18 July 2003.

Houghton Mifflin Company, The American Heritage® Dictionary of the English Language, 4th Edition. Copyright © 2000, by Houghton Mifflin Company

International Panel on Climate Change (IPCC), Climate Change 2001, The Scientific Basis, Cambridge University Press, New York, 2001.

Joussaume, Sylvie, Three-dimensional simulations of the atmospheric cycle of desert dust particles using a general circulation model, *J. Geophys. Res.*, Vol. 95, No. D2, pp. 1,909-1,949, 1990.

Kuciauskas, Arunas P., S.D. Miller, and D.K. Westphal, Tactical application of a satellite-derived optical depth product during dust storm events in support of Operation Iraq Freedom, Proceedings from the Battlefield Atmospheric and Cloud Impacts of Military Operations (BACIMO) Conference, Monterey, CA, 9-11 Sept. 2003,

Mahrer Y., and R.A. Pielke, A numerical study of airflow over irregular terrain, *Buitrage zur Physik derAtmopshare*, Vol. 50, pp. 98-113, 1977.

Mellor, G.L., and T. Yamada, Development of a turbulence closure model for geophysical fluid problems, *Rev. Geophys. Space Phys.*, Vol. 20, pp. 851-875, 1982.

Meyers, M.P., R.L. Walko, J.Y. Harrington, W.R. Cotton, New RAMS cloud microphysics parameterization, Part II: The two-moment scheme, *Atmos. Res.*, Vol. 45, pp. 3-39, 1997.

Mie, G. Beiträge zur optic trüber medien spieziell kolloidaler metallösungen, *Ann. Phys.*, Vol. 25, 377-445, 1908

Miller, R.L., J. Perlwitz and I. Tegen, Feedback upon dust emission by dust radiative forcing through the planetary boundary layer, *J. Geophys. Res.*, Vol. 109, No. D24, 21 December 2004.

Mishchenko, M.I., L.D. Travis, R.A. Kahn and R.A. West, Modeling phase functions for dustlike tropospheric aerosols using a shape mixture of randomly oriented polydisperse spheroids, *J. Geophys. Res.*, Vol. 102, No. D14, pp. 16,831-16,847, 27 July 1997.

Myhre, G. and F. Stordal, Global sensitivity experiments of the radiative forcing due to mineral aerosols, *J. Geophys. Res.*, Vol. 106, No. D16, pp. 18,193-18,204, 27 August 2001.

Pollack, J.B. and J.N. Cuzzi, Scattering by Nonphserical Particles of Size Comparable to Wavelength: A New Semi-Emperical Theory and Its Application to Tropospheric Aerosols, *J. Atmos. Sci.*, Vol. 37, pp. 868-881, 1980.

Pruppacher, H.R., and J.D. Klett, *Microphysics of Clouds and Precipitation*, D. Riedel Publ. Co., Dordrecht Holland, 714pp., 1978.

Qian, Y., L.R. Leung, S.J. Ghan and F. Giorgi, Regional climate effect of aerosols over China: modeling and observation, *Tellus*, Vol. 55B, pp. 914-934, 2003.

Ramanathan, V., P.J. Crutzen, J.T. Kiehl, and D. Rosenfeld, Aerosols, Climate and the Hydrological Cycle, *Science*, Vol. 294, pp. 2,119- 2,124, 7 December 2001.

Randall, D.A., Geostrophic Adjustment and the Finite-Difference Shallow-Water Equations, *Mon. Wea. Rev.*, Vol. 122, pp. 1,371-1,377, June 1994.

Ritter, B. and J-F. Geleyn, A Comprehensive Radiation Scheme for Numerical Weather Prediction Models with Potential Application in Climate Situations, *Mon. Wea. Rev.*, Vol. 120, pp. 303-325, February 1992.

Saleeby, S.M., and W.R. Cotton, A Large Droplet Mode and Prognostic Number Concentrations of Cloud Droplets in the Colorado State University Regional Atmospheric Modeling System (RAMS). Part I: Module Descriptions and Supercell Test Simulations, *J. Appl. Meteor.*, Vol. 43, pp. 182-195, January 2004.

Schauer, J.J., W.F. Rogge, L.M. Hildermann, M.A. Mazurek, G.R. Cass and B.R.T. Simoneit, Source apportionment of airborne particulate matter using organic compounds as tracers, *Atmos. Environ*, Vol. 30, pp. 1,578-1,587, 1999.

Seinfeld, J.H. and S.N. Pandis, *Atmospheric Chemistry and Physics*, Wiley-Interscience, New York, USA, 1998.

Slingo, A. and H.M. Schrecker, On the shortwave properties of stratiform water clouds, *Quart. J. R. Met. Soc.*, Vol. 108, pp. 407-426, 1982.

Smagorinsky, J., General circulation experiments with the primitive equations. Part I: The basic experiment, *Mon. Wea. Rev.*, Vol. 94, pp. 99-164, 1962.

Sokolik, I.N, and O.B. Toon, Direct radiative forcing by anthropogenic airborne mineral aerosols, *Nature*, Vol. 381, pp. 681-683, 20 June 1996.

Streets, D.G., T.C. Bond, T. Lee and C. Jang, On the future of carbonaceous aerosol emissions, *J. Geophys. Res.*, Vol. 109, No. D24, 28 December 2004.

Tanre, D., J. Haywood, J. Pelon, J.F. Leon, B. Chatenet, P. Formenti, P. Francis, P. Goloub, E.J. Highwood, G. Myhre, Measurements and modeling of the Saharan dust radiative impact: Overview of the Saharan Dust Experiment (SHADE), *J. Geophys. Res.*, Vol. 108, No. D18, 6 August 2003.

Tegen, I., A.A. Lacis, and I. Fung, The influence on climate forcing of mineral aerosols from disturbed soils, *Nature*, Vol. 380, pp. 419-422, 4 April, 1996.

Trembeck, C.J., Numerical Simulations of a mesoscale convective complex: Model development and numerical results. PhD Dissertation, Atmos. Sci. paper no. 465, Colorado State University, Department of Atmospheric Science, Fort Collins, CO, 1990.

Tripoli, G.J. and W.R. Cotton, The Colorado State University three-dimensional cloud/mesoscale model-1982. Part I: General theoretical framework and sensitivity experiments, *J. Rech. Atmos.*, Vol. 16, pp. 185-220, 1985.

Tripoli, G.J. and W.R. Cotton, An intense quasi-steady thunderstorm over mountainous terrain. Part IV: Three-dimensional numerical simulation, *J. Atmos. Sci.*, Vol. 43, No. 9, pp. 894-913, 1986.

Twomey, S. Influence of pollution on the short-wave albedo of clouds, *J. Atmos. Sci.*, Vol. 34, No. 7, pp. 1149-1152, 1977

van den Heever, S.C., G.G. Carrio, W.R. Cotton, W.C. Straka, The impacts of Saharan dust on Florida thunderstorm characteristics, AMS Conference on Planned and Inadvertent Weather Modification, Vol. 16, 2005.

Verlinde, J, P.J. Flatau and W.R. Cotton, Analytical solutions to the collection growth equation: Comparison with approximate methods and applications to cloud microphysics parameterization schemes, *J. Atmos. Sci.*, Vol. 47, pp. 2,871-2,880, 1990.

Walko, R.L., W.R. Cotton, M.P. Meyers, J.Y. Harrington, New RAMS cloud microphysics parameterizations, Part I: the single moment scheme, *Atmos. Res.*, Vol. 38, pp. 29-62, 1995.

Yu, H., R.E. Dickinson, M. Chin, Y.J. Kaufman, M. Zhou, Y. Tian, O. Dubovik, and B.N. Holben, Direct radiative effect of aerosols as determined from a combination of MODIS retrievals and GOCART simulations, *J. Geophys. Res.*, Vol 109, No. D3, 12 February 2004.